

# Determining the Timing and Rate of Southeastern Laurentide Ice Sheet Thinning During the Last Deglaciation with $^{10}\text{Be}$ Dipsticks

Christopher T Halsted

A thesis  
submitted to the Faculty of  
the department of Earth and Environmental Sciences  
in partial fulfillment  
of the requirements for the degree of  
Master of Science

Boston College  
Morrissey College of Arts and Sciences  
Graduate School

© Copyright (2018) Christopher T Halsted

**DETERMINING THE TIMING AND RATE OF SOUTHEASTERN LAURENTIDE ICE SHEET THINNING DURING THE LAST DEGLACIATION USING <sup>10</sup>Be DIPSTICKS**

Christopher T Halsted

Advisor: Jeremy D. Shakun, Ph.D.

Abstract

The deglacial extent chronology of the southeastern Laurentide Ice Sheet as it retreated through the northeastern United States and southern Quebec has been well constrained by multiple lines of evidence. By comparison, few data exist to constrain the thinning history of the southeastern Laurentide, resulting in lingering uncertainty about volume changes and dynamics of this ice mass during the deglacial period. To address the lack of thinning information, my team collected 120 samples for *in-situ* <sup>10</sup>Be exposure dating from various elevations at numerous mountains in New England and southern Quebec. Monte Carlo regression analyses using the analytical uncertainties of exposure ages from each mountain are used to determine the most-likely timing and rate of ice thinning for that location, a technique known as the ‘dipstick approach’.

While this larger project is ongoing, I have processed and measured <sup>10</sup>Be concentrations of 42 samples for this thesis and present my preliminary results and interpretation here. Exposure ages from Peekamoose Mt. in southern NY suggest ice thinning early in the deglacial period (~19.5 – 17.5 ka), near the onset of the Heinrich Stadial I cold period. Samples from Franconia Notch, NH, and Mt. Mansfield, VT, suggest ice thinning from approximately 15 – 13 ka in northern New England, roughly coincident with the Bølling-Allerød warm period. Exposure ages from each of the northern New England dipsticks are nearly identical within 1σ internal uncertainty, indicating that ice thinning was rapid. Higher elevation (>1200 m a.s.l.) samples

from the northern New England mountains appear to contain inherited  $^{10}\text{Be}$  from previous periods of exposure, indicating a lack of glacial erosion on these surfaces. My high-elevation samples with inherited  $^{10}\text{Be}$  suggest that these summit landscapes were preserved beneath cold-based, non-erosive ice during the last glacial and deglacial periods. 40 samples that have yet to be processed will provide more information on ice thinning around Killington Mt., VT, Mt. Greylock, MA, Mt. Bigelow, ME, and Mt. Jacques-Cartier, Quebec. Ultimately, this information will be used to create probabilistic reconstructions of the lowering southeastern Laurentide ice surface during its retreat.

## ACKNOWLEDGEMENTS

There are many people who I would like to thank for their involvement with this project, but I especially want to thank Jeremy Shakun for being not only a mentor, but a friend. Jeremy introduced me to this project, guided me through all aspects of it, and supported me the whole way. Without him I would not have had the opportunity to pursue such incredible research. I also want to extend a special thank you to Paul Bierman and Lee Corbett at the University of Vermont. Not only did they let me use their state-of-the-art cosmogenic nuclide production lab for two months straight, they helped me through an extraordinarily difficult part of this project. Thank you to Jahan Ranezani for the use of the rock crushing and sieving facilities at MIT, and to Ken Galli for keeping up with my constant need for acid waste removal from Boston College. Thank you to Marc Caffee and the staff at the Purdue Rare Isotopes Measurement lab for measuring our  $10/9\text{Be}$  ratios. Thank you to Noah Snyder and Ethan Baxter for serving as committee members for my thesis. Thanks to Anthony (Cole) Vickers and Allie Koester for their assistance with sample collection. Thanks to Thom Davis and David Dethier for field assistance as well as their shared knowledge about New England glaciation. Thank you to the entire Boston College department of Earth and Environmental Sciences. Funding for this project was received from NSF award EAR-1603175.

# TABLE OF CONTENTS

<b>Table of Contents .....</b>	<b>v</b>
<b>List of tables .....</b>	<b>vii</b>
<b>List of figures .....</b>	<b>viii</b>
<b>1. Introduction .....</b>	<b>1</b>
<b>2. Background .....</b>	<b>6</b>
<b>2.1 Cosmogenic Nuclide Exposure Dating .....</b>	<b>6</b>
2.1.1 Theory .....	6
2.1.2 Exposure Age Calculations .....	9
2.1.3 Production Rate Estimation .....	9
2.1.4 Potential Complications and Sources of Inaccurate Exposure Ages .....	10
<b>2.2 Deglacial Paleoclimate and the Retreat of the Southeastern LIS .....</b>	<b>12</b>
2.2.1 The Bi-Polar See-Saw Hypothesis.....	12
2.2.2 Pre-Last Glacial Maximum .....	15
2.2.3 The Last Glacial Maximum .....	16
2.2.4 Last Glacial Maximum to Heinrich Stadial I .....	16
2.2.5 Heinrich Stadial I .....	17
2.2.5.1 Southern Hemisphere Climate during HS1 .....	17
2.2.5.2 Northern Hemisphere Climate during HS1 .....	19
2.2.6 Bølling-Allerød Warm Period .....	20
2.2.6.1 Meltwater Pulse 1a .....	20
2.2.6.2 Southeastern LIS Retreat During the Bølling-Allerød .....	21
2.2.7 Younger Dryas .....	22
<b>2.3 Laurentide Ice Sheet Thinning History .....</b>	<b>23</b>
<b>3. Research Motivations .....</b>	<b>24</b>
<b>4. Research Objectives .....</b>	<b>27</b>
<b>5. Methods .....</b>	<b>28</b>
<b>5.1 Field Work .....</b>	<b>28</b>
5.1.1 Sample Collection .....	28
5.1.2 Dipstick Locations .....	28
5.1.2.1 Peekamoose Mt., NY .....	28
5.1.2.2 Wachusett Mt., MA .....	29
5.1.2.3 Mt. Greylock, MA .....	29
5.1.2.4 Killington Mt., VT .....	30
5.1.2.5 Jay Peak, VT .....	31
5.1.2.6 Mt. Bigelow, ME .....	32
5.1.2.7 Franconia Notch, NH .....	32
5.1.2.8 Mt. Mansfield, VT .....	32

<b>5.2</b>	<b>Sample Processing</b>	<b>33</b>
5.2.1	Mineral Separation	34
5.2.2	Chemical Processing/Be Extraction	34
<b>5.3</b>	<b>Calculating <math>^{10}\text{Be}</math> Exposure Ages</b>	<b>35</b>
5.3.1	Conversion of $^{10}\text{Be}/^9\text{Be}$ Ratio to $^{10}\text{Be}$ Concentrations	35
5.3.2	Process Blank Calculations	37
5.3.3	Calculating the Exposure Age	38
<b>5.4</b>	<b>Dipstick Creation</b>	<b>38</b>
<b>6.</b>	<b>Results</b>	<b>40</b>
6.1	Difficulties in Mineral Separation	40
6.2	Calculated Exposure Ages and Dipsticks	43
6.2.1	Peekamoose Mt., NY	43
6.2.2	Wachusett Mt., MA	43
6.2.3	Mt. Greylock, MA	44
6.2.4	Killington Mt., VT	44
6.2.5	Jay Peak, VT	45
6.2.6	Mt. Bigelow, ME	45
6.2.7	Franconia Notch, NH	46
6.2.8	Mt. Mansfield, VT	47
<b>7.</b>	<b>Discussion</b>	<b>48</b>
7.1	Interpretation of exposure age outliers	48
7.1.1	Anomalously old, pre-LGM exposure ages	48
7.1.2	Anomalously young Holocene exposure ages	49
7.1.3	Anomalous deglacial exposure ages	50
7.2	General Trends	51
7.2.1	Overlapping Exposure Ages	51
7.2.2	North-South Trend	51
7.3	Timing of southeastern LIS thinning	51
7.3.1	Early Thinning (19.5-17.5 ka)	51
7.3.2	Heinrich Stadial I Thinning (~17.6 – 14.6 ka)	52
7.3.3	Bølling-Allerød Thinning (~14.6 – 12.9 ka)	53
7.4	Rate of southeastern LIS thinning	54
7.5	Comparison to Present-Day Thinning in Greenland and Antarctica	55
7.6	Future Work	55
<b>8.</b>	<b>Conclusion</b>	<b>57</b>

## LIST OF TABLES

<b>Table 1.</b> Acronyms used in this thesis.	68
<b>Table 2.</b> Organic $^{14}\text{C}$ age-elevation pairs from the White Mountains, NH.	69
<b>Table 3.</b> $^{10}\text{Be}$ exposure ages of New England dipstick samples.	69
<b>Table 4.</b> Measured $^{10}\text{Be}$ concentrations and calculated exposure ages for New England dipstick samples.	70
<b>Table 5.</b> Mt. Mansfield samples collected and processed by Lee Corbett, Paul Bierman, Thom Davis, Jeremy Shakun, and Allie Koester.	72
<b>Table 6.</b> The onset of exposure at each dipstick location based on Monte Carlo simulations.	72

## LIST OF FIGURES

<b>Figure 1.</b> A recent reconstruction of the Laurentide Ice Sheet at its maximum extent.	73
<b>Figure 2.</b> Map of dipstick sample locations in New England.	74
<b>Figure 3.</b> Visualization of an incident primary cosmic particle and the secondary cosmic particle cascade.	75
<b>Figure 4.</b> A simplified depiction of the dipstick method.	76
<b>Figure 5.</b> Proxy records of benthic temperature and Atlantic Meridional Overturning Circulation strength.	77
<b>Figure 6.</b> A benthic foraminifera oxygen-isotopic record compared to July insolation at 65°N over the past 1 million years.	78
<b>Figure 7:</b> Global eustatic sea level reconstruction of the last 35 kyr.	79
<b>Figure 8:</b> Constraints on the southeastern LIS retreat history through New England.	80
<b>Figure 9:</b> Time distance plot of LIS recession up the Connecticut Valley based on the new North American Varve Chronology.	81
<b>Figure 10:</b> Embedded pebbles in a conglomerate boulder from the eastern Catskill Mountains, NY.	82
<b>Figure 11:</b> A prominent quartz vein from the summit of Jay Peak, VT.	83
<b>Figure 12:</b> Example of a prominent quartz vein on Mt. Mansfield, VT.	84
<b>Figure 13:</b> Results of Monte Carlo dipstick simulations using exposure ages from the Catskill Mountains, NY.	85
<b>Figure 14:</b> Results of Monte Carlo dipstick simulations using exposure ages from Mt. Greylock, MA.	85
<b>Figure 15:</b> Results of Monte Carlo dipstick simulations using exposure ages from Killington Mt., VT.	86
<b>Figure 16:</b> Exposure ages from Jay Peak, VT.	86
<b>Figure 17:</b> Franconia Notch sample locations.	87

<b>Figure 18:</b> Exposure ages from Franconia Notch, NH.	88
<b>Figure 19:</b> Results of Monte Carlo dipstick simulations using exposure ages from Franconia Notch, NH.	88
<b>Figure 20:</b> Exposure ages on Mt. Mansfield, VT.	89
<b>Figure 21:</b> Results of Monte Carlo dipstick simulations using exposure ages from Mt. Mansfield, VT.	90
<b>Figure 12:</b> Preliminary dipsticks in the northeastern United States.	91

## 1 INTRODUCTION

At the heart of modern sustainability efforts is a belief in intergenerational equity, that future generations are entitled to the same environmental and economic stability that we ourselves inherited. One of the principle threats to intergenerational equity is that past and present anthropogenic greenhouse gas emissions are altering the climate system, with potentially disastrous consequences for future generations. While science and policy discussions of anthropogenic climate impacts have largely remained focused on projections to the year 2100 AD, affecting only the next few human generations, a growing body of evidence has generated a consensus that 20<sup>th</sup> and 21<sup>st</sup> century greenhouse gas emissions will result in long-term, irreversible climate change, with effects lasting more than 10,000 years (Friedlingstein et al., 2011; Clark et al., 2016).

The long residence time of CO<sub>2</sub> perturbations in the atmosphere (Archer et al., 2009; Eby et al., 2009) and the clear evidence linking past CO<sub>2</sub> increases to global warming and ice sheet retreat (Denton et al., 2010; Clark et al., 2012; Shakun et al., 2012; Heinemann et al., 2014) have particularly raised concerns about the long-term future stability of the Greenland and Antarctic Ice Sheets (Robinson et al., 2012; Nick et al., 2013; Kleman and Applegate, 2014). Currently storing 7 and 58 m of sea level rise, respectively, the decay of vulnerable portions of these ice bodies represents one of the biggest threats to future generations, with the potential to displace nearly 19% of the world's population (using 2010 population statistics, Clark et al., 2016). Accurately predicting the rate and total, long-term volume of ice loss from Greenland and

Antarctica due to anthropogenic climate perturbations is therefore of paramount importance to climate change mitigation and adaptation policy discussions.

Presently, however, projections of ice sheet stability contain significant uncertainty. The Intergovernmental Panel on Climate Change, for example, gives a most-likely range for global mean sea level rise by 2100 AD due to ice sheet contribution of 0.26 to 0.98 m (Stocker et al., 2014). Other experts have insisted that this estimate is too low, arguing that Antarctica alone could contribute more than a meter of sea level rise by the 22<sup>nd</sup> century (DeConto and Pollard, 2016). In a controversial publication, Jim Hansen, former head of the NASA Goddard Institute for Space Studies, argued for even more extreme projections, stating that multi-meter sea level rise is almost guaranteed in the next 50-150 years with unabated emissions (Hansen et al., 2016).

These large uncertainties are due primarily to a limited understanding and poor model representation of ice sheet marginal processes such as ice-stream flow, ice-shelf buttressing, and subglacial meltwater drainage (Kleman and Applegate, 2014; Stokes, 2017). The processes at work in these marginal regions are key components of an ice sheet's mass balance and serve as the interface between the ice sheet and other components of the climate system such as the atmosphere and oceans (Applegate et al., 2012). Today, many state-of-the-art ice sheet models, such as the SICOPOLIS model (e.g. Little et al., 2007; Robinson et al., 2012), use what is called the 'shallow-ice approximation' to solve for the evolution of ice thickness during decay (Greve and Blatter, 2009). This approximation, which simplifies the shear stress experienced by the base of the ice sheet, can reliably reproduce ice sheet thinning dynamics over most interior regions of terrestrial ice sheets, but fails in areas of interest to stability analyses such as ice streams and ice shelves at ice margins (Applegate et al., 2012). Accurately modelling the behavior of these areas is difficult because modern observations in Greenland and Antarctica (e.g. Pritchard et al., 2009)

capture only a brief window in their history. Furthermore, important basal processes are nearly impossible to observe on modern ice sheets. These limitations prevent current ice sheet models from replicating so-called ‘instability events’ observed in reconstructions of former ice sheets, short periods in which the ice sheets rapidly purged mass from their interiors to ablating or calving margins (Kleman and Applegate, 2014).

Studying past ice sheets to understand the mechanisms of ice sheet decay and the interactions between ice sheets and other components of the climate system offers a potential solution to observational limitations. Evidence indicating how former ice margins behaved during retreat is particularly valued, as ice sheet models are usually unable to replicate their movements (Greve and Blatter, 2009; Applegate et al., 2012; Robinson et al., 2012). Numerous geologic indicators of ice extent are incorporated into most reconstructions of former ice sheets, building on decades of effort (see Stokes et al., 2015 for a comprehensive list of reconstructions and methods) aimed at depicting the decay of the ice sheets present at the Last Glacial Maximum (LGM; Table 1 describes all acronyms used in this thesis).

However, while the areal retreat histories of most LGM ice sheets have been investigated with numerous geomorphic and geochemical methods, the thinning histories of these ice sheets are almost wholly unconstrained. This is largely due to a lack of suitable methods with which to reconstruct past ice sheet thicknesses. Published geophysical models of ice thickness based on inverted isostatic rebound patterns disagree considerably (e.g. Clark and Tarasov, 2014; Peltier et al., 2015), and numerical model simulations of ice thickness evolution based on paleoclimate change contain substantial amounts of uncertainty (e.g. Gregoire et al., 2012; Abe-Ouchi et al., 2015). The uncertainty surrounding the thinning histories of LGM ice sheets has propagated to other areas of paleoclimate, limiting our understanding of meltwater pulse events (e.g. Liu et al.,

2016), ice-ocean-atmosphere interactions (e.g. Ullman et al., 2014), and abrupt climate change events (e.g. Carlson and Clark, 2012; Gregoire et al., 2012).

A relatively novel approach to constraining ice-thinning histories is the ‘dipstick’ method, where a series of cosmogenic nuclide exposure ages are taken at a range of elevations in areas of significant topography (see commentary by Bierman, 2007). The theory behind the method is that as LGM ice sheet surfaces lowered, they exposed more and more topography, and by taking exposure ages from a range of elevations in one location, the lowering ice surface can essentially be tracked through time. This method has been used to constrain the thinning history of the Scandinavian (Goehring et al., 2008); Antarctic (Stone et al., 2003; Ackert et al., 2007; Mackintosh et al., 2011; Johnson et al., 2014), and Greenland (Corbett et al., 2011) Ice Sheets, but has seen limited use with the Laurentide Ice Sheet (LIS, Fig 1). To date, only three dipsticks have been developed for the LIS (Davis et al., 2015; Koester et al., 2017; Koester et al. *in prep*), despite the fact that the LIS was the largest Northern Hemisphere ice sheet at the LGM (Clark and Mix, 2002; Abe-Ouchi et al., 2015; Stokes, 2017).

The purpose of this thesis project is to greatly expand the LIS dipstick dataset. Unfortunately, the LIS predominately covered flat terrain over the interior regions of the northern United States and Canada, limiting the areas where dipsticks can be produced. While the eastern Canadian Arctic provides sufficient topographic relief for dipstick construction, its polar climate may have been conducive to non-erosive ice during the last glacial period (Sugden, 1978; Briner et al., 2003), reducing the effectiveness of the dipstick method (see section 5 for more detail). Therefore, New England is the only region with the necessary topography and paleoclimate for successful LIS dipstick construction.

In this project, I aim to develop dipsticks from nearly a dozen mountains in New England (Fig. 2). It should be noted that this project is a multi-year undertaking with a scope beyond that of a typical master's thesis. As such, the focus of this thesis is on the processing, preliminary results, and preliminary interpretation of a subset ( $n = 42$  samples) of the expected total New England dipstick dataset ( $n = 120$  samples). Many of the remaining samples are not currently processed, but data from these samples are expected in the next year as I begin a PhD with Dr. Paul Bierman at the University of Vermont, with this project as one of my initial focuses. By generating a dataset of exposure age dipsticks in New England, I hope to shed light on the interactions between the southeastern LIS, deep ocean convection, and abrupt climate change during the last deglacial period,  $\sim 21 - 11$  thousand years ago (ka). Ultimately, I hope to improve the glaciological community's understanding of ice sheet decay and the interactions between ice sheets and other elements of the climate system.

## 2 BACKGROUND

### 2.1 *Cosmogenic Nuclide Exposure Dating*

#### 2.1.1 Theory

Terrestrial *in-situ* cosmogenic nuclides (TCNs) are isotopes created during nuclear reactions between terrestrial atoms and high energy cosmic rays. They have been used to analyze a variety of surface processes since the development of accelerator mass spectrometry made their detection and measurement possible (Gosse and Phillips, 2001). Davis and Schaeffer (1955) originally noted that rocks continually exposed to cosmic rays become progressively more irradiated at a rate dependent on the cosmic ray flux at that location. They realized that by measuring the present concentration of a TCN in a rock, estimating the TCN production rate, and accounting for atomic decay if the TCN is radioactive, the exposure age of that rock could be calculated.

Subsequent research revealed that the production rate of TCNs can be affected by a multitude of parameters, including latitude, elevation, and depth below the surface. The source of TCNs are primary cosmic rays; streams of high-energy, positively charged particles originating from supernova explosions mainly within the Milky Way galaxy (Ackermann et al., 2013). Despite the variation in TCN production rates observed at Earth's surface, the flux of primary cosmic rays is believed to have remained relatively constant over the last 10 million years (Caffee et al., 1988; Vogt et al., 1990). As they approach the Earth, the primary cosmic ray flux is modulated by the geomagnetic field according to the Lorentz force, which dictates that a charged particle traversing a magnetic field will be deflected normal to both the direction of motion and the field (Lemaitre and Vallarta, 1933). Earth's geomagnetic field, with field lines

nearly parallel to Earth's surface at the equator and perpendicular to the surface at the poles, deflects lower-energy cosmic particles away from the Earth at lower latitudes, resulting in a pattern of increasing primary cosmic ray flux with latitude (Gosse and Phillips, 2001).

The primary cosmic particles that do reach Earth's upper atmosphere collide with atmospheric atoms almost immediately. These collisions, called spallation reactions, break apart the atmospheric atoms and create a cascade of secondary particles (Fig. 3) that shoot away from the point of collision with high energies. The nucleonic component of this secondary cosmic particle cascade (neutrons primarily) collide with and rip apart other atmospheric atoms, expanding the cascade. Due to the large number of atoms in the atmosphere, almost none of the primary cosmic ray flux makes it to sea level. Instead, the flux of high-energy secondary cosmic particles entirely replaces the primary cosmic ray flux within the atmosphere (Dunai, 2010).

With increasing atmospheric depth, the flux of secondary cosmic particles decreases exponentially, as more and more atmospheric reactions decrease the average energy of the secondary cascade (Gosse and Phillips, 2001). Therefore, given two surfaces at the same latitude, the one at a higher elevation will experience a higher overall cosmic ray flux and have higher TCN production rates. Complicating matters is the fact that cosmic rays can be blocked by high topography around a sample site. For example, given two surfaces at the same elevation and latitude, a surface surrounded by high mountains will receive fewer incident secondary cosmic particles than a surface surrounded by flat fields. Finally, the secondary cosmic particles that reach the Earth's surface with high energy collide with terrestrial atoms in crystal matrixes, producing TCNs (Gosse and Phillips, 2001; Dunai, 2010).

As in the atmosphere, the cosmic flux in the solid Earth decreases approximately exponentially with depth, as collisions between the secondary cosmic particles and terrestrial

atoms reduce the energy of the cosmic flux. The depth at which the production rate of TCNs decreases by a factor of  $e^{-1}$ , a property known as the attenuation length, is determined by the density of the substance through which it is traveling. For a crystalline bedrock material such as granite ( $\rho \approx 2.6 \text{ g cm}^{-3}$ ) the cosmic flux, and TCN production, is negligible below about 2 m depth (Gosse and Phillips, 2001).

With latitude, elevation, and local topography all affecting the incident cosmic ray flux at any given location, determining the TCN production rate for a sample is difficult and usually includes some uncertainty. Lal (1991) created a set of equations, known as a scaling scheme, which factors in these parameters to estimate the production rate for TCNs at a particular location using a calibration data set as reference. A calibration is created by measuring the TCN concentration of samples with independently-known exposure histories, allowing the time-averaged TCN production rate of the sample to be precisely calculated. The scaling schemes introduced by Lal (1991) extrapolate what the TCN production rates may be at a sample location by calculating how differences in latitude, elevation, and topographic shielding between a calibration site and the sample would affect the incident cosmic ray flux. This technique appears to be effective at extrapolating production rates to new sample locations, but it has been shown that the closer a calibration data set is to the sample location, the more accurate and precise the scaled production rate will be (e.g. Balco et al., 2009).

Phillips, Elmore, and others (1986) were among the first to attempt TCN exposure dating using accelerator mass spectrometry, and Nishiizumi and others (1991) were the first to apply it to glacial chronologies, which have since become one of the most widely practiced applications of TCN exposure dating. TCNs have become such successful tools for glacial chronologies primarily because of the erosional nature of warm-based glaciers and ice sheets. If an ice body is

sufficiently thick to lower the pressure melting point at its base below the ambient basal temperature, melt occurs and forms a lubricating layer of water on which the glacier can slide. Warm-based ice sheets can easily remove  $\geq 2$  m of bedrock, exposing minerals at the surface that were previously shielded from cosmic radiation (Balco, 2011). These surficial minerals only begin accumulating TCNs when the overlying ice retreats and exposes them to cosmic rays. Consequently, surface exposure ages from glacially-polished bedrock or glacially-transported boulders correspond to the date of ice retreat from that location.

### 2.1.2 Exposure Age Calculations

Cosmogenic nuclide surface exposure ages are calculated by measuring the current concentration of the target nuclide in surficial minerals ( $N$ , atoms  $\text{g}^{-1}$ ) and estimating the rate at which the nuclide accumulated in the minerals during their exposure ( $P$ , atoms  $\text{g}^{-1} \text{yr}^{-1}$ ). Accounting for the decay constant of radioactive nuclides ( $\lambda$ ,  $\text{yr}^{-1}$ ), the time of exposure ( $t$ , yr) can be calculated using Equation 1:

$$\text{Eq. 1} \quad N_{10} = \frac{P_{10}}{\lambda_{10}} [1 - e^{-\lambda_{10}t}] \quad (\text{Balco, 2011})$$

Where the '10' subscripts in this case refer to  $^{10}\text{Be}$ , the TCN used for this project. The steps that follow describe the processes involved in estimating  $P_{10}$  and calculating  $N_{10}$ .  $\lambda_{10}$  is generally given as  $4.99 \times 10^{-7} \text{yr}^{-1}$  (Balco, 2011).

### 2.1.3 Production Rate Estimation

$^{10}\text{Be}$  is used widely in glacial chronologies due to the ubiquitous nature of its host mineral, quartz, the low natural background concentration of all isotopes of Be in quartz (Dunai, 2010), and the relative confidence in estimations of its production rate due to the availability of

$^{10}\text{Be}$  calibration data sets (e.g., Balco et al., 2009). As discussed in section 2.1.1, the production rate ( $P$ ) of TCNs is affected by several parameters, all of which must be determined at sample sites to estimate  $P_{10}$  at each location. Generally, a handheld GPS provides latitude, longitude, and elevation data, and an inclinometer and Brunton compass are used as tools to determine topographic shielding and surface attitude. Before 2008, this data would have been entered into numerical models designed to estimate the local  $P_{10}$  (Gosse and Phillips, 2001). In 2008, Greg Balco and others released free online software designed to take site parameters as input and run the numerical models on a central server, making  $P_{10}$  estimations far more accessible and easier to calculate (Balco et al., 2008). One of the true strengths of this software (called CRONUS-Earth: <http://hess.ess.washington.edu/>), is that it is also a repository for published regional calibration studies, producing  $P_{10}$  estimates with low uncertainty where a regional calibration rate is available. Additionally, the increased use of this software by the cosmogenic community has standardized exposure age calculations, allowing direct age comparisons without complications from different age calculation methods.

In the northeastern US, a regional calibration data set has been constructed by reconciling  $^{10}\text{Be}$  exposure ages on glacial features with independently constrained ages based on the North American Varve Chronology (Balco et al., 2009; Ridge et al., 2012).  $P_{10}$  estimates calculated using this regional calibration data set (available on CRONUS-Earth: [http://hess.ess.washington.edu/math/al\\_be\\_v22/alt\\_cal/alt\\_cal.html](http://hess.ess.washington.edu/math/al_be_v22/alt_cal/alt_cal.html)) were shown to have less internal scatter than estimates using the global  $^{10}\text{Be}$  calibration, leading to increased accuracy in exposure ages. The lower uncertainty in  $^{10}\text{Be}$  exposure ages in New England is the primary reason why it was the TCN chosen for this study.

#### **2.1.4 Potential Complications and Sources of Inaccurate Exposure Ages**

Cosmogenic nuclide exposure dating is a robust method for constraining a variety of surficial processes, but there are some mechanisms that can produce inaccurate exposure ages. Because  $^{10}\text{Be}$  production attenuates with depth, a sample surface that has been covered by significant amounts of material (e.g. till, seasonal snow, relict ice) following glacial recession will accumulate less  $^{10}\text{Be}$  than a surface that has been constantly exposed, producing an apparently younger exposure age. Careful selection of sample surfaces can help mitigate this effect. For example, the top surface of a large boulder is less likely to have been covered by snow or till than a nearby bedrock surface. A potential cause of inaccurate exposure ages for glacially-transported boulders is post-depositional movement. Again, careful evaluation of a sample can mitigate this risk. Ideal boulders for this project are generally located far from steep slopes or on local topographic high points. Another cause of inaccurate exposure ages that primarily affects bedrock samples is the presence of inherited TCNs. Because of its  $\sim 1.4$  million-year half-life, little  $^{10}\text{Be}$  decays over glacial-interglacial cycles. Therefore, if a surface was overridden by non-erosive ice and the  $\sim 2$  m of bedrock containing  $^{10}\text{Be}$  atoms from previous exposures was not removed, measured  $^{10}\text{Be}$  concentrations today will be higher than fresh surfaces first exposed following ice retreat.

One method that is used to determine if boulders experienced post-glacial movement or if bedrock contains inherited  $^{10}\text{Be}$  is to sample boulders and bedrock near each other as pairs. The top surface of boulders rarely contains inherited  $^{10}\text{Be}$  due to the strong likelihood that they were eroded, transported, and overturned at some point during the glaciation. Conversely, bedrock surfaces will not experience movement of any kind and will not be eroded by cold-based ice cover. Therefore, if either (or both) of the samples in the pair has an exposure age that has been

affected by these mechanisms, it is unlikely that they will be affected in the same way. Furthermore, if the two ages in the pair agree, it lends confidence to each age.

## **2.2 *Deglacial Paleoclimate and the Retreat of the Southeastern Laurentide Ice Sheet***

For reading clarity and efficiency, it may have been wise to discuss separately the paleoclimate of the deglacial period and the retreat of the southeastern margin of the LIS (which retreated through New England). However, these two histories are intimately linked and the evolution of one is often directly caused by changes in the other. Therefore, I discuss the evolution of the deglacial paleoclimate and the retreat of the southeastern LIS margin together. This section is broken into sub-sections corresponding to established, climatically-defined intervals observed in paleoclimate records of the deglacial period. Before beginning this discussion, however, it is useful to first introduce the ‘bi-polar see-saw’ hypothesis – a leading idea to explain the pattern of climate change in the North Atlantic during the deglacial period, and its connection to climate changes elsewhere around the world.

### **2.2.1 The Bi-Polar See-Saw Hypothesis**

Perhaps second only to the dominant overall deglacial signal from ~25-11 ka, one of the most important features of late-Pleistocene (100 – 11 ka) North Atlantic paleoclimate is a series of abrupt climate changes observed in Greenland ice cores (Dansgaard et al., 1993; Cuffey and Clow, 1997; Grootes and Stuiver, 1997; Johnsen et al., 2001). A potential mechanism for these millennial-scale warming and cooling episodes was proposed by Broecker, Peteer, and Rind in 1985. They argued that changes in the strength of the Atlantic Meridional Overturning Circulation (AMOC) caused the North Atlantic (and possibly more regions as well) to rapidly shift between two quasi-stable modes of climate (Broecker et al., 1985).

Put simply, the AMOC is the transport of warm, salty, surface water northward in the Atlantic Ocean, culminating in the sinking of this water and the formation of North Atlantic Deep Water (NADW) at high northern latitudes. NADW then moves southward at intermediate depths, ultimately completing a loop by rising to the surface in the Southern Ocean and moving north once more. The AMOC is unique in two respects: (1) it features the only site of deep-water formation in the Northern Hemisphere, and (2) it transports heat northward at all latitudes in the Atlantic, including latitudes south of the equator. Because of these features, surface water in the northern North Atlantic is about 4°C warmer than water found in the northern Pacific Ocean (Rahmstorf, 1996).

The hypothesis put forth by Broecker et al. (1985) suggested that during periods of glacial buildup, the export of freshwater from the North Atlantic decreased due to reduced evaporation, resulting in reduced salt content in North Atlantic waters and a reduction in the formation of NADW. This had the effect of slowing the AMOC and reducing heat transport into the North Atlantic, further cooling the climate in this region and reducing freshwater export more. This reduced AMOC state was one of their proposed quasi-stable modes of climate; and had two primary consequences: (1) the reduced heat transport into the North Atlantic resulted in lower temperatures in Greenland, western Europe, and eastern North America, and (2) the reduced export of heat from the South Atlantic resulted in higher temperatures in this region. The antiphase nature of temperature changes in the Northern and Southern Hemispheres led to this pattern being dubbed the ‘bi-polar see-saw’ (Broecker et al., 1985).

In interglacial periods, like the present, the AMOC is in a ‘strong’ state due to an imbalance of evaporation over precipitation/freshwater runoff in the North Atlantic, resulting in higher than average salinity in this region and promoting the formation of NADW. This is the

other quasi-stable mode of the bi-polar see-saw proposed by Broecker et al. (1985), and results in higher temperatures in the North Atlantic (as seen today relative to the North Pacific), and cooler temperatures in the South Atlantic.

This thesis focuses on events during the last deglaciation (~25 – 11 ka), an interval in which the AMOC played a significant climatic role in northeastern North America and the North Atlantic region. Paleoclimate evidence suggests that during this period, the AMOC frequently oscillated between its ‘weak’ and ‘strong’ modes (Fig. 5; McManus et al., 2004; Thornalley et al., 2010). Broecker et al. (1985) proposed that the melting of continental ice sheets near the North Atlantic produced a massive freshwater flux that may have reduced NADW production by rendering surface waters less saline and therefore less dense. This caused the AMOC to oscillate to its ‘weak’ state, reducing temperatures in the North Atlantic and slowing ice retreat. The subsequent reduction of freshwater entering the North Atlantic caused salt to build up once more, increasing the density of surface waters and re-initiating the formation of NADW. This caused the AMOC to oscillate back to its ‘strong’ state, warming temperatures in the North Atlantic and accelerating ice retreat, starting the cycle over again. In the years following Broecker et al. (1985), numerous lines of paleoclimatic evidence have supported their initial hypothesis of quasi-stable AMOC modes and a bi-polar see-saw (e.g. McManus et al., 2004; Barker et al., 2009; Thornalley et al., 2010; see Alley, 2007 for a comprehensive list of studies).

Clark et al. (2001) expanded the hypothesis of Broecker et al. (1985), describing a mechanism that could explain the timing of the AMOC oscillations observed during the last deglaciation. Using modeled reconstructions of LIS meltwater runoff patterns (Marshall and Clarke, 1999; Licciardi et al., 1999), Clark et al. (2001) hypothesized that when LIS meltwater is directed primarily down the Mississippi River and discharged into the Gulf of Mexico, it had a

strengthening effect on the AMOC. Alternatively, if LIS meltwater was diverted through eastern drainage outlets, such as the Hudson River, St. Lawrence River, or Hudson Strait, the influx of freshwater to the North Atlantic suppressed thermohaline circulation and the formation of NADW, causing the AMOC to oscillate to its ‘weak’ mode. Clark et al. (2001) argued that the direction and strength of the primary LIS meltwater flux was controlled by the location of its margins, which exposed certain drainage outlets as they retreated and sometimes prevented meltwater drainage, creating large proglacial lakes.

In the following sections, specific evidence is given where available to illustrate how the mechanism of the bi-polar see-saw and the direction and strength of the LIS meltwater flux may have interacted during the last deglacial period. It should be noted that recent observations suggest that the AMOC is currently declining in strength (Caesar et al., 2018; Thornalley et al., 2018), which is perhaps a response to rising atmospheric CO<sub>2</sub> and increased freshwater runoff from the Canadian Arctic and Greenland (Saba et al., 2016). Understanding prior interactions between the AMOC and meltwater from shrinking ice sheets is important for evaluating the future risk of AMOC changes in the face of anthropogenic climate change.

### **2.2.2 Pre-Last Glacial Maximum**

The growth of Northern Hemisphere ice sheets following the last interglacial period (~122 ka) was likely triggered by a change in the orientation of Earth’s axis, part of a Milankovich precessional cycle, that coincided with large orbital eccentricity around 115 ka. Climate and ice sheet models indicate that the new orbital configuration caused summer insolation at high northern latitudes (also known as boreal summer insolation, or BSI) to decrease, which forced a positive mass balance of ice in the Canadian high Arctic. Although two subsequent precessional cycles at ~104 and 84 ka resulted in orbital configurations that increased

BSI (Fig. 6), the ongoing reduction of orbital eccentricity from the last interglacial muted these BSI maxima, and the ice sheet in the Canadian Arctic experienced a mostly positive mass balance for the next ~60 kyr, growing to become the LIS (Abe-Ouchi et al., 2013).

### **2.2.3 The Last Glacial Maximum (~29 – 21 ka)**

As the global average, or eustatic, sea level (for the duration of this thesis, ‘sea level’ will mean eustatic sea level unless otherwise indicated) is directly influenced by the size of continental ice sheets, the global LGM is generally defined as coinciding with the last sea level minimum (Clark and Mix, 2002; Clark et al., 2009; Lambeck et al., 2014). However, terminal moraine dates from around the world (Clark et al., 2009) indicate that individual ice sheet margins did not necessarily reach their maximal positions in-sync with the last sea level minimum around 21 ka (Fig. 7; Fairbanks et al., 1989; Bard et al., 1990; Chappell and Polach, 1991; Peltier and Fairbanks, 2006; Bard et al., 2010; Deschamps et al., 2012; Lambeck et al., 2014). Therefore, in this thesis the LGM will refer the period in which the southeastern margin of the LIS was at its maximum extent, defined by terminal moraines in Martha’s Vineyard, Massachusetts ( $29.2 \pm 1.7$  ka; Fig. 8; Balco et al., 2002), and northern New Jersey ( $25.2 \pm 1.3$  ka; Corbett et al., 2017). The difference in dates for ice retreat and the stratigraphic evidence within these moraines suggests that the southeastern LIS ice margin may have experienced small fluctuations but remained near its maximum position for 3-4 kyrs (Balco et al., 2002).

### **2.2.4 LGM to Heinrich Stadial I (~21 – 17.6 ka)**

BSI rose following the last eccentricity and precession minimums around 24 ka (Carlson and Winsor, 2012), slowly initiating the retreat of Northern Hemisphere ice sheets. Global temperature change lagged the rise in BSI, but a gradual Northern Hemisphere temperature increase that started around 21.5 ka is believed to be due primarily to the shift in insolation

forcing (He et al., 2013). The gradual Northern Hemisphere warming continued from 21.5-19 ka, a period characterized by a strong AMOC (McManus et al., 2004; Shakun et al., 2012) and the continued retreat of the southern margins of most Northern Hemisphere ice-sheets (Clark et al., 2009). The LIS was one of the few ice sheets that did not undergo large-scale marginal retreat during this period (Stokes, 2017). The southeastern margin retreated a small amount from Martha's Vineyard to Buzzard's Bay by  $21.0 \pm 1.0$  ka (Balco et al., 2002), while the inland southern margin experienced an equally minor retreat (Dyke, 2004). Therefore, if the LIS contributed substantially to the estimated 10 m of ESL rise from 21.5-19 ka (Fig. 7; Lambeck et al., 2014), it would have done so primarily through thinning.

Kinematic proxy records indicate that the AMOC strengthened following the global LGM, but around 19 ka it began to rapidly weaken (Fig. 5; McManus et al., 2004; Ritz et al., 2013). Clark et al. (2001) argued that a rerouting of LIS meltwater from the Mississippi River to the newly-exposed Hudson River outlet was responsible for this decline, as the shift in freshwater injection to the North Atlantic suppressed the formation of NADW. This explanation is supported by proxy evidence from a sediment core in the North Atlantic, which found that meltwater rerouting coincided with an abrupt decrease in heat flux into the region (Thornalley et al., 2010).

### **2.2.5 Heinrich Stadial I (~19 – 14.6 ka)**

The AMOC reduction that began around 19 ka had profound effects on global climate, tipping the bi-polar see-saw and initiating the Heinrich Stadial 1 period (HS1) in the Northern Hemisphere (Liu et al., 2009; Denton et al., 2010; Clark et al., 2012). The AMOC reduction had several consequences in both hemispheres, which will be discussed separately below.

#### **2.2.5.1 Southern Hemisphere Climate during HS1**

The reduced northward Atlantic heat transport that started around 19 ka initiated interstadial conditions in the Southern Hemisphere. While Northern Hemisphere ice sheets had begun an initial stage of retreat due to rising BSI between 21.5-19 ka, full-glacial conditions persisted in much of the Southern Hemisphere through 19 ka (Denton et al., 2010). Surface air temperatures rose 4-5°C in the South Atlantic between 19-17.6 ka as AMOC strength and northward heat transport were reduced. This warming in conjunction with Northern Hemisphere cooling shifted the Intertropical Convergence Zone and the southern westerly wind belt to the south, leading to a reduction in sea-ice at mid-southern latitudes (Barker et al., 2009; Denton et al., 2010). Northward Ekman transport produced by the shifted southern westerlies is hypothesized to have increased upwelling in the Southern Ocean, which led not only to further reductions in sea ice but also to a release of CO<sub>2</sub> into the atmosphere (Denton et al., 2010).

It should be noted that the Southern Hemisphere response to the weakening of the AMOC was not instantaneous. Proxy records show that warming of high southern latitudes, including much of Antarctica, lagged the AMOC reduction by ~1 kyr (Shakun et al., 2012). The upwelling-driven atmospheric CO<sub>2</sub> increase also lagged the AMOC reduction, only appearing in proxy records ~17.5-17 ka (Liu et al., 2009; Clark et al., 2012; Shakun et al., 2012). Shakun et al. (2012) hypothesized that the high southern latitude temperature lag was due to the thermal inertia of the Southern Ocean, while the CO<sub>2</sub> response was delayed because it required a threshold to be exceeded in southern wind displacement and sea ice reduction. The rest of HS1 was characterized by rising temperatures in the Southern Hemisphere (Barker et al., 2009), a continued rise of atmospheric CO<sub>2</sub> levels, and retreat of Antarctic sea ice (Shakun et al., 2012), but as this thesis focuses on the LIS in the Northern Hemisphere, I will not discuss the chronology of Southern Hemisphere temperature rise and ice retreat in HS1 any further.

#### 2.2.5.2 Northern Hemisphere Climate during HS1

As oceanic heat was bottled up in the Southern Hemisphere, the North Atlantic experienced a reduction in surface temperatures that signaled the beginning of HS1. It has been hypothesized that the onset of stadial conditions in the North Atlantic between 19-17.6 ka resulted in an expansion of winter sea-ice, resulting in extremely low winter surface air temperatures ( $\sim 32^{\circ}\text{C}$  colder than today) and a highly seasonal climate (Broecker, 2006a; Denton et al., 2010). Despite the frigid North Atlantic winters, the North American Varve Chronology (Ridge et al., 2012) indicates that the southeastern LIS margin continued to retreat steadily through New England during HS1, interrupted only by a brief readvance around 17.4 ka (Fig. 9). This counter-intuitive pattern might be a consequence of the extreme seasonality that characterized North Atlantic climate during HS1. While AMOC variability is hypothesized to have had significant effects on winter surface air temperatures due to its direct influence on sea-ice extent, summer temperatures appear to have been less impacted (Broecker, 2006a). Buizert et al. (2014) estimated that North Atlantic summer temperatures during HS1 may have only been about  $8^{\circ}\text{C}$  colder than today. As summer surface air temperatures are the primary control on ice sheet volume (Abe-Ouchi, 2013), the retreat rates of the southeastern and southern LIS margins may have been minimally affected by the AMOC reduction during HS1 (Dyke, 2004).

The contribution of the LIS to sea level rise during HS1 is difficult to ascertain due to the lack of ice-thinning constraints and the onset of Antarctic melting during this period.

Reconstructions indicate that sea level rose  $\sim 25$  m from 19-16.5 ka (Fig. 7; Carlson and Clark, 2012; Lambeck et al., 2014), however Ullman et al. (2015) argued that the meltwater flux from the LIS decreased during this period as southern low-angle marginal lobes retreated, diminishing the ablation area of the LIS. The continued retreat of the southeastern margin during HS1 could

have contributed to the 25 m sea level rise, but a largely Southern Hemisphere source is still implied in the literature (Denton et al., 2010; Shakun et al., 2012).

### **2.2.6 Bølling-Allerød Warm Period (~14.6-12.9 ka)**

Around 15 ka, proxy records indicate that the AMOC rapidly increased in strength (Fig. 5; McManus et al., 2004; Ritz et al., 2013), an event that has been attributed to a redirection of LIS meltwater from the Hudson River to the Mississippi River (Clark et al., 2001; Carlson and Clark, 2012). The recovery of the AMOC had significant effects in the North Atlantic; it has been linked to a retreat of winter sea ice, reduced seasonality, and rapid Greenland warming (Liu et al., 2009; Denton et al., 2010; Carlson and Clark, 2012).

#### 2.2.6.1 Meltwater Pulse 1a

Around the time of, or shortly following, the increase in AMOC strength, sea level suddenly rose at extreme rates in a brief interval known as Meltwater Pulse 1a (MWP-1A). From ~14.6 - 14.3 ka, sea level rose between 8.6 - 14.6 m at a rate of 40 mm yr<sup>-1</sup> or greater, by far the fastest of the last deglaciation (Fig. 7; Deschamps et al., 2012; Lambeck et al., 2014; Liu et al., 2016). MWP-1A was originally thought to be sourced entirely from the LIS, as it was the largest ice sheet in the Northern Hemisphere at the onset of an interstadial (Peltier, 2005; Gregoire et al., 2012). However, evidence from LIS margins do not support this argument. Much of the southern LIS margin re-advanced or exhibited minimal retreat from 15-14 ka (Dyke, 2004; Carlson and Clark, 2012); and at the eastern LIS margin, iceberg discharge did not increase through the Gulf of St. Lawrence or Hudson Strait before or during MWP-1A (Carlson et al., 2012). In fact, only the southeastern LIS margin in New England exhibited substantial retreat during this period, accelerating to a 300 m yr<sup>-1</sup> retreat rate around the same time as the onset of MWP-1A (Fig. 8 & 9; Ridge et al., 2012; Carlson and Clark, 2012). Furthermore, relative sea level fingerprints and

uplift rates predicted from ice sheet models following the ‘LIS-only’ MWP-1A scheme fail to match data, indicating that this scenario may not be correct (Carlson and Clark, 2012).

Deschamps et al. (2012) argued that a better fitting scheme attributed half of the MWP-1A sea level rise to Antarctica. However, Liu et al. (2016) re-examined the proxy data from Deschamps et al. (2012), and other studies, and argued that uncertainties are too large to make any conclusive statements about the total Antarctic contribution to MWP-1A. While available sea-level data are unable to confidently constrain its source, a MWP-1A scheme with significant Antarctic contribution does a better job of explaining climatic events that occurred during and following the event. The AMOC, after having recovered to pre-HS1 strength by 14.6 ka, continued to strengthen, overshooting its pre-HS1 level by ~6 Sv by 14.35 ka (Fig. 5; McManus et al., 2004; Ritz et al., 2013). Weaver et al. (2003) simulated the AMOC response to different MWP-1A source scenarios and argued that a LIS-only source for this event would have significantly weakened the AMOC, whereas a large Antarctic contribution could produce the AMOC strengthening that is observed in the proxy record.

#### 2.2.6.2 Southeastern LIS Retreat During the Bølling-Allerød

Increased varve thickness in the Connecticut River Valley indicates that more meltwater was produced by the southeastern LIS during the Bølling-Allerød (B-A) than at any other point in its retreat (Ridge et al., 2012), suggesting that summer ablation increased substantially during this period. Increased ablation maintained the rapid ice margin retreat in New England until ~14.0 ka, when ice core records indicate that cooling occurred over Greenland and the North Atlantic, coinciding with an abrupt decrease in southeastern LIS meltwater production (Ridge et al., 2012). The Littleton-Bethlehem moraine complex in northern New Hampshire marks the point where the southeastern LIS re-advanced around 14 ka (Fig. 9; Ridge et al., 2012; Bromley

et al., 2015; Thompson et al., 2017). The Greenland ice core record indicates that this cool period lasted for about 200 years before North Atlantic temperatures suddenly increased again. At this time, the southeastern LIS resumed its northward retreat at a rate of  $\sim 150 \text{ m yr}^{-1}$ , retreating fully out of New Hampshire and Vermont by  $\sim 13.4 \text{ ka}$  (Fig. 8 & 9; Ridge et al., 2012).

### **2.2.7 Younger Dryas ( $\sim 12.9 - 11.7 \text{ ka}$ )**

Around 12.9 ka, a sudden AMOC reduction similar to that which initiated the HS1 stadial period (Fig. 5) led to an abrupt drop in North Atlantic temperatures, ending the B-A and ushering in a stadial period known as the Younger Dryas (Dyke, 2004; Broecker, 2006a; Carlson and Clark, 2012; Clark et al., 2012; Buizert et al., 2014). By this time, the LIS had retreated out of New England completely, (Fig. 8; Dyke, 2004; Ridge et al., 2012) so I will not discuss the movements of the LIS margin during this period or subsequent climatic changes beyond the onset of stadial conditions.

The cause of the AMOC reduction around 12.9 ka was initially hypothesized to be a rerouting of LIS meltwater to the newly exposed St. Lawrence river outlet (Broecker et al., 1989), however, more recent arguments in favor of a northern outlet through the Mackenzie River (Tarasov and Peltier, 2005; Condron and Winsor, 2012) now have robust proxy support (Keigwin et al., 2018). A horizon of detrital  $\text{CaCO}_3$  found in sediment cores near the Hudson Strait suggests that a large iceberg discharge event also occurred around the same time (Clark et al., 2001; Broecker, 2006b; Clark et al., 2012). The rerouted meltwater and iceberg discharge events around 12.9 ka likely injected a large volume of freshwater into the North Atlantic, which would have disrupted the formation of NADW and abruptly slowed the AMOC (Fig. 5; McManus et al., 2004; Tarasov and Peltier, 2005; Carlson and Clark, 2012; Clark et al., 2012).

### 2.3 *Laurentide Ice Sheet Thinning History*

While the retreat chronology of the LIS has been clearly defined in most areas using a variety of methods, data on its thinning history is sparse. Initial attempts to reconstruct a southeastern LIS thinning history produced  $^{14}\text{C}$  ages from lake and bog basal sediments in the White Mountains, NH, and Mt. Katahdin, ME, meant to determine minimum-limiting ages for the lowering of the ice surface in the region (Table 2; Davis and Davis, 1980; Spear, 1989; Spear et al., 1994; Rogers, 2003). However, the results contain so much scatter and uncertainty that they are of limited use in determining the timing and rate of ice thinning.

Preliminary cosmogenic exposure ages have yielded more conclusive results, with exposure-age dipsticks providing evidence of rapid ice thinning in central Maine (~16-15 ka; Fig. 5; Davis et al., 2015), the Presidential Range of New Hampshire (starting ~17 ka; Koester et al., *in prep*), and on the Maine coast ( $15.2 \pm 0.7$  ka; Fig. 5; Koester et al., 2017). It should be noted that the dipsticks from central and coastal Maine feature broad 90% confidence intervals, preventing the exclusion of more complex thinning histories with varying thinning rates. Furthermore, cosmogenic exposure ages from the highest summits in this region are anomalously old, likely due to the incomplete removal of cosmogenic nuclides from prior episodes of exposure by non-erosive, cold-based ice (Bierman et al., 2015; Koester et al., *in prep*). These high-elevation exposure ages, therefore, cannot be meaningfully interpreted because their cosmogenic nuclide concentrations do not reflect a single period of exposure (see Section 2.1.3).

The dipsticks reported by Davis et al. (2015) and Koester et al. (2017, *in prep*) are useful, but to extrapolate the timing and pattern of ice thinning observed at these locations to other areas of the LIS would involve significant uncertainty. Accurately reconstructing the thinning behavior of the entire southeastern LIS therefore requires more data covering a large geographic area.

### ***3.1 Constraining Individual Ice Sheet Volume Histories***

While the deglacial sea level history has been confidently reconstructed (Clark et al., 2009; Carlson and Clark, 2012; Lambeck et al., 2014), the sea level contributions of individual ice sheets through time is still poorly understood. This is due primarily to uncertainties in the thickness, and therefore volume, of individual ice sheets through the last deglaciation. These uncertainties prevent further understanding of the sources and mechanisms behind discrete meltwater pulse events observed in the deglacial sea level record (Fig. 4; Clark et al., 2002; Clark et al., 2004; Deschamps et al., 2012; Liu et al., 2016). Most of these meltwater events were marked not only by rapid ESL rise, but also by abrupt climate changes. MWP-1A in particular is associated with a rapid strengthening of the AMOC (McManus et al., 2005; Liu et al., 2009), the onset of the B-A, and accelerated retreat of the southeastern LIS margin (Dyke et al., 2004; Ridge et al., 2012; Stokes, 2017). Constraining the timing and rate of southeastern LIS thinning could provide valuable information to help advance understanding of this event.

### ***3.2 Understanding Interactions Between the LIS and Global Climate***

Constraining the timing and rate of LIS thinning is also important for our general understanding of the interactions between the LIS and other elements of the climate system during the last deglaciation. While AMOC strength generally appears to have responded to changes in the magnitude and direction of the LIS meltwater flux (Clark et al., 2001; Liu et al., 2009), a causal relationship between the two variables has not been established due to a lack of constraints on the LIS volume through time. By refining the southeastern LIS thinning history, this relationship may become clearer.

### **3.3 *Improving Confidence and Accuracy in Deglacial Paleoclimate Models***

The height of the LIS is an essential boundary condition for deglacial paleoclimate models (e.g. Barron and Pollard, 2002; Ullman et al., 2014). Ullman et al. (2014) showed that a 20% difference in LIS elevation at the LGM, the difference between published reconstructions by Peltier (2004) and Toscano et al. (2011), resulted in substantial differences in model simulations of the deglacial paleoclimate. Glacial orography has an outsized effect on climate for several reasons. The height of an ice sheet has a direct effect on surface air temperatures through vertical lapse rate, but it also affects atmospheric circulation, with higher ice sheets acting as larger impediments to upper-atmosphere flow (Bromwich et al., 2004; Abe-Ouchi et al., 2007; Langen and Vinther, 2009). The effect of this flow impediment is a re-organization of the atmospheric jet, which has downstream effects on mid-latitude storm tracks and wintertime precipitation across much of the NH (Ullman et al., 2014). LIS thickness is also believed to affect the strength of the AMOC, both through its effect on wind stress in the Atlantic (Arzel et al., 2008) and its meltwater flux volume and direction (Clark et al., 2001; Ullman et al., 2014). Present uncertainties about the thickness of the LIS therefore introduce significant uncertainty into paleoclimate models of the last deglacial period.

### **3.4 *Improved Understanding of Ice Margin Dynamics***

Finally, an accurate, measurement-based three-dimensional reconstruction of the southeastern LIS would prove useful to ice-sheet modelers trying to replicate the behavior of retreating ice margins. While many state-of-the-art ice sheet models can reliably reproduce observed dynamics over interior regions of ice sheets, they fail in these marginal areas (Greve and Blatter, 2009; Robinson et al., 2012), introducing uncertainty into projections of future stability (Applegate et al., 2012).

Recent geomorphic evidence suggests that the southeastern LIS drained into the Atlantic Ocean through several ice streams, some of which occupied present-day New England and southern Quebec (Margold et al., 2015; Stokes, 2017). Additionally, the ice in this region was almost certainly buttressed by ice shelves that extended into the Atlantic (Stokes, 2017). This makes the southeastern LIS retreat through New England a useful case study for the behavior of complex marginal ice systems in a warming world.

## 4 RESEARCH OBJECTIVES

The motivations behind this project help frame its discrete objectives:

(1) Determine the timing and rate of ice thinning at various latitudes throughout New England. Due to the lack of ice thickness reconstructions, there is substantial uncertainty in the timing and pace of ice thinning in this region, which has consequences for paleoclimate models and understanding of ice-ocean-climate interactions.

(2) Determine, if possible, whether the southeastern LIS thinning rate varied during its deglaciation. The last deglacial period encompassed several warm and cold periods, but currently available thinning histories cannot discern if regional climate influenced the thinning rate of the southeastern LIS. Of particular interest is the behavior of the southeastern LIS around the time of MWP-1A.

(3) Re-examine the relationship between southeastern LIS volume changes and AMOC strength. By using an empirically-based ice thinning history, the mechanisms at work between these two systems can hopefully be examined with greater detail and confidence.

(4) Compare my empirically-based ice thinning history to isostatic rebound-based reconstructions (e.g. Clark and Tarasov, 2014; Peltier et al., 2015) and ice-sheet model simulations (e.g. Gregoire et al., 2012; Abe-Ouchi et al., 2013). Such reconstructions and models have been limited by the lack of geologic constraints, a problem that this project could reduce.

## 5 METHODS

### 5.1 *Field Work*

#### 5.1.1 **Sample Collection**

Samples for this project are 1-5 cm thick rock fragments taken from the top surface of bedrock and boulders. Rock fragments were collected using a chisel and hammer, and site parameters were recorded using a handheld GPS unit (latitude, longitude, elevation), a Brunton compass (surface attitude), and an inclinometer (topographic shielding).

#### 5.1.2 **Dipstick Locations**

To capture as much of the southeast LIS thinning history as possible, the locations selected to create  $^{10}\text{Be}$  dipsticks for this project are prominent peaks spread throughout New England, southern New York, and southern Quebec (Fig. 2).

##### 5.1.2.1 *Peekamoose Mountain, NY*

The Catskill Mountains of southern New York (Fig. 2) are an uplifted, dissected plateau of Devonian age, whose bedrock is composed primarily of siliciclastic sedimentary rocks. Bedrock lithologies become more fine-grained from east to west, with pebble and gravel conglomerates near the eastern edge of the Catskills transitioning into sandstones and shales in the west (Ver Straeten, 2013). Because of this, samples were sought in the eastern Catskills, where glacially transported, conglomerate boulders contain embedded 2-6 cm quartz pebbles (Fig. 10).

Five samples were collected from Peekamoose Mountain (Table 3). Three samples were collected from the summit area, all with elevations greater than 1100 m above sea level (asl), and two samples were collected down-trail from the summit at around 900 m asl. Each sample

consisted of several quartz pebbles embedded on the surface of a conglomerate boulder, under the assumption that each pebble had almost identical exposure histories to its neighbors on the surface of the boulder, and together they could be treated as a single sample.

#### 5.1.2.2 Wachusett Mountain, MA

Wachusett Mountain (Fig. 2) is part of the Fitchburg plutonic complex, a series of metamorphosed igneous sheets in central Massachusetts and southern New Hampshire. At 611 m asl, Wachusett Mountain is the highest point in the Fitchburg complex, which is characterized otherwise by rolling hills reaching no more than ~400 m asl. Wachusett is composed mainly of foliated biotite-granodiorite-tonalite gneiss, which is overlain by the Littleton Formation (gray-weathering schists and quartzites) and massive to weakly foliated biotite-muscovite granite at the summit. Acadian metamorphism created significant chemical variations observed at outcrops around Wachusett (Maczuga, 1981; Zen et al., 1983).

With a vertical relief of 306 m, Wachusett Mountain is expected to capture only a brief window in the southeastern LIS thinning history. Wachusett's value is in its location; it is the highest peak in central Massachusetts and is surrounded by mostly flat terrain, making it the only feasible location to construct a dipstick in southeastern New England.

Four samples were collected from Wachusett at roughly 60 m elevation increments (Table 3). All samples come from large boulders that appear to be composed of local gneiss. Samples were sought at Wachusett's exposed summit, but the presence of abundant human activity, including a radio tower, an access road, and a parking lot indicated a high risk of human interference. Because of this risk, no summit samples were collected from the summit of Wachusett.

#### 5.1.2.3 Mt. Greylock, MA

Mount Greylock is geologically part of the Taconic Mountains but is located near the Berkshire Mountains of northwestern Massachusetts (Fig. 2). It is the tallest mountain in the state, with a summit elevation of 1064 m asl and a vertical relief of 751 m. Mt. Greylock is composed primarily of metamorphized sedimentary rock, including marble, which is overlain by schist and phyllite of the Taconic allochthon (Bierman and Dethier, 1986). Mount Greylock is the product of thrust faulting during the Taconic orogeny, which thrust the Ordovician phyllite and schist over the dolomitic marble (Ratcliffe et al., 1993).

Nine samples were collected from Mt. Greylock. MG-01 and -02 were sampled from boulders near the summit composed of the Ordovician phyllite characteristic of the upper reaches of Greylock. MG-03, -04, and -06 were sampled from bedrock quartz veins near the summit, 900 m asl, and 780 m asl. MG-05 and -07 were sampled from boulders at 770 and 900 m asl respectively, and also seem to be composed of local phyllite. MG-08 and -09 were sampled from large quartzite boulders located to the north of Mt. Greylock, at around 400 m asl. These boulders were probably sourced from a nearby outcrop but were located sufficiently far from the outcrop to have most likely been transported by glacial action rather than rock fall.

#### 5.1.2.4 Killington Mt., VT

Killington Mt. (Fig. 2) is the tallest mountain in southern Vermont, with a summit elevation of 1288 m asl. Killington is part of the Green Mountain range, which runs north-south for the entire length of Vermont, extending north into Quebec as the Sutton Mountains and south into Massachusetts as the Berkshire Mountains. The Green Mountains were formed in the Acadian Orogeny, a major mountain building event in the Devonian that shaped many of the ranges that comprise the modern-day Appalachian chain. Killington Mt. is primarily comprised

of garnetiferous quartzite, a highly metamorphosed sandstone containing 60 to 90 percent quartz (Brace, 1953).

Nine samples were collected along a vertical transect of Killington Mt. (Table 3). Four of the samples (KM-01 through-04) were taken from prominent bedrock quartz veins near the exposed summit, while the other five samples (KM-05 through -09) came from boulders of native bedrock lithology at lower elevations. Killington is characterized by steeper slopes (15-20°) on the upper third of the mountain, introducing a potential for incorrect boulder ages due to a higher likelihood of post-glacial movement. Samples KM-05 and KM-06 were located on these steeper slopes, whereas samples KM-07 and -08 came from lower elevations, where the slope became gentler (5-10°). Sample KM-09 was taken from a boulder located at the base of Killington, in a flat area that may have been a glacial outwash surface. Exposed bedrock was absent from lower elevations, prohibiting a boulder-bedrock pair sampling strategy.

#### 5.1.2.5 Jay Peak, VT

Jay Peak is a prominent peak in northern VT (Fig. 2) surrounded primarily by low rolling hills, making it an ideal sampling location to capture large-scale ice thinning. Jay Peak was formed by Devonian thrust faulting, which placed a fine-grained, quartz-chlorite-albite phyllitic schist and quartzite unit (called the Jay Peak Formation) over the predominantly graphitic schist found elsewhere in the region (Doolan, 2017). The Jay Peak Formation contains remarkable, prominent quartz veins (Fig. 11), several of which were sampled for dipstick construction.

Thirteen samples were collected from Jay Peak, including three quartz veins at the exposed summit (1176 m asl, JP-01 to -03) and one 90 m below (JP-08). Like Killington Mt., exposed bedrock was absent from lower elevations, so all samples between 295-1060 m asl are from boulders.

#### 5.1.2.6 Mt. Bigelow, ME

Mt. Bigelow is actually a large east-west running ridgeline comprised of several peaks in northwestern Maine (Fig. 2). The ridgeline is composed primarily of Devonian-age pelites of varying chemical composition that were pushed up during synclinal folding in the Acadian orogeny (Osberg et al., 1985).

Mt. Bigelow is characterized by a steep flank, limiting the availability of suitable boulder samples (i.e., not located on steep slopes) at mid-elevations. Because of this, samples were taken from boulders (BP-01 and -03) and bedrock (BP-02, -04, and -05) on the ridgeline and from two boulders near the base (BP-06 and -07). All boulders appear to be composed of the native pelitic lithology.

#### 5.1.2.7 Franconia Notch, NH

Franconia Notch is a glacially-carved valley in the White Mountains region of New Hampshire (Fig. 2 & 16). The entire notch, as well as most of the White Mountain region, is comprised of Conway Granite, a Jurassic-age plutonic intrusion with a characteristic pink color (Lyons et al., 1997), making it ideal for dipstick construction due to the abundance of quartz.

The Franconia samples come from several locations in the notch, including Mt. Lafayette, Little Haystack Mountain, Artist's Bluff, and the valley floor. In total, 16 samples were collected, with most from boulders but a few from bedrock outcrops (LFT-17, LFT-14, and LFT-13) (Fig. 16). Samples from the valley floor, particularly samples FN-01 and FW-01, are located below steep slopes and as such have a higher probability of having experienced post-glacial rolling.

#### 5.1.2.8 Mt. Mansfield, VT

Mt. Mansfield is the tallest mountain in Vermont (Fig. 2). Like many other mountains in the Green Mountain chain, its bedrock is a Cambro-Ordovician age (500-380 million years ago) mica-albite-quartz schist formed from metamorphism of sediment from an ancient shallow sea (Christman, 1956). The metamorphism of these ancient sediments resulted in the formation of prominent quartz veins observed frequently on Mt. Mansfield (Fig. 12). Like Mt. Lafayette in Franconia Notch, the size of Mt. Mansfield and the abundance of quartz available on the mountain make it an ideal location for dipstick construction.

Efforts to construct a Mt. Mansfield dipstick were already underway before I joined this project; Lee Corbett, Paul Bierman, P. Thompson Davis, Jeremy Shakun, and Alexandra Koester collected 15 samples above 1000 m asl (Fig. 19; samples labeled as 'L/P/T'). To complement this dataset, I collected 10 more samples from lower elevations on Mt. Mansfield. All of my samples except for MM-17 and -18 were collected from boulders of the local schist lithology and ranged in elevation from 920 – 410 m asl. MM-17 and -18 were taken from prominent quartz veins observed in bedrock outcrops on Mt. Mansfield. MMB-01, -02, and -03 were taken from boulders resting on a flat surface about a half mile away from the base of Mt. Mansfield. These samples were collected at this location to ensure that the boulders from which they were taken did not arrive there via post-glacial rolling.

## **5.2 *Sample Processing***

As the target TCN for this project is  $^{10}\text{Be}$  in quartz, sample processing comprises mineral and chemical separation techniques designed to isolate quartz from the host matrix and then extract Be from the quartz.

### **5.2.1 Mineral Separation (after Corbett et al., 2016)**

Samples are first crushed, ground, and sieved to obtain sediment in the 850-250  $\mu\text{m}$  size range. This sediment is then repeatedly etched in a 1% HF/HNO<sub>3</sub> solution, which dissolves the other mineral constituents in the sample but leaves most of the durable quartz particles intact. This method was first developed by Kohl and Nishiizumi (1992) and requires that each crushed sample be separated into 50 gram aliquots, placed in 4-liter containers with the 1% acid solution, and allowed to sit in a sonicator for at least 24-hours. Kohl and Nishiizumi (1992) found that this ratio of sample-size, acid strength, and container size produced the most effective quartz isolation with minimal quartz loss, especially when repeated up to three times and followed by weaker, longer acid etches. This chemical method of mineral separation is usually preceded by a physical mineral separation method, such as magnetic separation, density separation, or froth flotation (Somasundaran, 1975), to reduce the number of acid etches needed to remove accessory minerals from the sample. Rapid inductively coupled plasma optical emission spectrometry (ICP-OES) is used to test an aliquot of the extracted quartz for purity. An aliquot with >150 ppm Al and >300-400 ppm cations is considered 'impure' and undergoes another week of acid etches.

### **5.2.2 Chemical Processing/Be Extraction (after Corbett et al., 2016)**

The extracted, pure quartz from each sample is then digested in concentrated HF (~5 g HF per g quartz), and a <sup>9</sup>Be carrier is added to the solution. At the University of Vermont Cosmogenic Nuclide Lab, where these samples were chemically processed, this carrier is made in-house from deep-mined beryl and is almost entirely composed of <sup>9</sup>Be. One of the assumptions in <sup>10</sup>Be exposure dating is that the sample quartz has no native <sup>9</sup>Be, so any <sup>9</sup>Be measured in the sample by an AMS is attributed entirely to the carrier added during chemical processing. This is typically a valid assumption, as non-cosmogenic Be is rare in quartz, but there have been

projects that have had to deal with high levels of native  $^9\text{Be}$  in samples (e.g., Portenga et al., 2015). In these cases, the total mass of  $^9\text{Be}$  in a sample must be calculated by measuring the  $^9\text{Be}$  concentration in two differently-sized aliquots of quartz using ICP-OES and taking the average concentration to estimate the concentration of  $^9\text{Be}$  in the sample (Portenga et al., 2015). At the University of Vermont Cosmogenic Nuclide Lab, ICP-OES analysis after mineral separation and prior to the addition of a carrier can detect the presence of native  $^9\text{Be}$ , providing a check on the validity of this assumption.

Following dissolution of quartz and addition of the  $^9\text{Be}$  carrier, samples are heated to evaporate HF and then fumed with perchloric acid to remove fluoride compounds. Subsequent centrifuging removes Ti and insoluble fluorides. Samples are then converted to chloride form via dissolution in HCl for anion column chromatography to remove Fe. HCl is subsequently evaporated and samples are converted to sulfate form for cation column chromatography, which removes B and Ti and separates Be from Al. Another rapid ICP-OES analysis is employed at this point to check the samples for yield and purity. Samples are then precipitated as  $\text{BeO}_2$ , dried, and converted to BeO via intense heating with an air/wall gas flame. Finally, samples are packed into stainless steel cathodes for AMS analysis after being mixed with Nb at a 1:1 ratio.

### **5.3 *Calculating $^{10}\text{Be}$ Exposure Ages***

#### **5.3.1 Conversion of $^{10}\text{Be}/^9\text{Be}$ Ratio to $^{10}\text{Be}$ Concentrations**

Following mineral separation and chemical processing, samples are sent to the Purdue Rare Isotopes Measurement (PRIME) lab for AMS analysis. This form of mass spectrometry uses a particle accelerator in conjunction with a mass spectrometer to isolate the ion beam and discard interferences. This allows the AMS to detect single atoms of the desired mass in the

presence of  $1 \times 10^{15}$  other atoms (Hellborg and Skoq, 2008). The AMS at the PRIME lab is used exclusively to measure mass ratios between cosmogenic nuclides ( $^{10}\text{Be}$  in this case) and a stable isotope added to the sample as a carrier ( $^9\text{Be}$ ). The concentration of  $^{10}\text{Be}$  in each quartz sample ( $N_{10}$ ) is then calculated using the following equation:

$$\text{Eq. 2} \quad N_{10} = \frac{1}{M_q} \left( \frac{R_{10/9} M_C N_A}{A_{Be}} - n_{10.B} \right) \quad (\text{Balco, 2006})$$

Where  $M_q$  is the mass of the quartz sample (g),  $R_{10/9}$  is the measured ratio of  $^{10}\text{Be}/^9\text{Be}$  (unitless),  $M_C$  is the mass of  $^9\text{Be}$  added as carrier (g),  $N_A$  is Avogadro's number ( $6.022 \times 10^{23}$  atoms mol $^{-1}$ ),  $A_{Be}$  is the molar weight of Be (9.012 g mol $^{-1}$ ), and  $n_{10.B}$  is the number of  $^{10}\text{Be}$  atoms measured in a process blank. A process blank is included with every batch of samples because stray  $^{10}\text{Be}$  atoms can be introduced during chemical processing and within the AMS. The blank undergoes the same chemical processing and measurement procedures as the other samples in the batch, so any  $^{10}\text{Be}$  that has accumulated in the blank is assumed to have accumulated in all other samples and is subtracted during the concentration calculation (discussed in more detail in section 5.3.2.).

Uncertainty in the  $^{10}\text{Be}$  concentration comes from three sources: the uncertainty in the isotope ratio measurement ( $\sigma R_{10/9}$ ), the uncertainty in the number of atoms measured in the process blanks ( $\sigma n_{10,B}$ ), and the uncertainty in the mass of  $^9\text{Be}$  added as a carrier ( $\sigma M_C$ ). The uncertainty in the  $^{10}\text{Be}$  concentration ( $\sigma N_{10}$ ) is therefore calculated as:

$$\text{Eq. 3} \quad \sigma N_{10} = \sqrt{\left( \frac{\partial N_{10}}{\partial R_{10/9}} \sigma R_{10/9} \right)^2 + \left( \frac{\partial N_{10}}{\partial n_{10,b}} \sigma n_{10,b} \right)^2 + \left( \frac{\partial N_{10}}{\partial M_C} \sigma M_C \right)^2} \quad (\text{Balco, 2006})$$

with:

$$\begin{aligned}\frac{\partial N_{10}}{\partial R_{10/9}} &= \frac{M_C N_A}{M_q A_{Be}} \\ \frac{\partial N_{10}}{\partial n_{10,B}} &= \frac{-1}{M_q} \\ \frac{\partial N_{10}}{\partial M_C} &= \frac{R_{10/9} N_A}{M_q A_{Be}}\end{aligned}$$

However, recent advancements in the development and addition of  $^9\text{Be}$  carriers, especially those made in-house at the University of Vermont, have made the carrier mass uncertainty so negligible that it adds very little uncertainty to the concentration and can be removed from the entire equation without much impact.

### 5.3.2 Process Blank Calculations

The process blanks in each batch of samples undergo the same chemical processing and measurement procedures as the samples themselves, and the AMS produces a  $^{10}\text{Be}/^9\text{Be}$  ratio for each blank. The equations given above require an estimate of the number of  $^{10}\text{Be}$  atoms on the blank, which is given by:

$$\text{Eq. 4} \quad n_{10,B}^* = \frac{R_{10/9} M_C N_A}{A_{Be}} \quad (\text{Balco, 2006})$$

Where  $R_{10/9}$  is now the  $^{10}\text{Be}/^9\text{Be}$  ratio measured in the blank. The uncertainty in the estimated number of  $^{10}\text{Be}$  atoms in the blank is:

$$\text{Eq. 5} \quad \sigma n_{10,B}^* = \sqrt{\left(\frac{\partial n_{10,B}^*}{\partial R_{10/9}} \sigma R_{10/9}\right)^2 + \left(\frac{\partial n_{10,B}^*}{\partial M_C} \sigma M_C\right)^2} \quad (\text{Balco, 2006})$$

where:

$$\begin{aligned}\frac{\partial n_{10,B}^*}{\partial R_{10/9}} &= \frac{M_C N_A}{A_{Be}} \\ \frac{\partial n_{10,B}^*}{\partial M_C} &= \frac{R_{10/9} N_A}{A_{Be}}\end{aligned}$$

Again,  $\sigma R_{10/9}$  is the uncertainty in the  $^{10}\text{Be}/^9\text{Be}$  ratio measured in the blank. As in Eq. 3, the uncertainty in the mass of  $^9\text{Be}$  added as a carrier ( $\sigma M_C$ ) is so negligible that it is taken to be 0, eliminating the second source of uncertainty in Eq. 5.

### 5.3.3 Calculating the Exposure Age

Using Eq. 1, the CRONUS-Earth software can calculate exposure ages if the concentration of  $^{10}\text{Be}$  and associated uncertainty is provided for each sample along with the sample site parameters (Balco et al., 2008). The software provides not only the exposure age of each sample, but also the internal and external uncertainties of the age. Internal uncertainty is derived from  $\sigma N_{10}$ , reflecting measurement uncertainties during chemical processing and AMS measurement. External uncertainty is a measure of the uncertainty in both  $P_{10}$  and  $N_{10}$ . While both sources of uncertainty are important, every exposure age in a single dipstick has consistent uncertainty due to  $P_{10}$  estimates, because they are located in close proximity to each other, with only elevation changing between sample sites. Therefore, differences in internal uncertainty are of primary concern for constructing dipsticks. External uncertainty is used when comparing glacial chronologies based on TCN exposure ages to chronologies based on other methods.

To reduce external uncertainties, all exposure ages for this project were calculated using the Northeastern North America calibration data set, which produces lower  $\sigma P_{10}$  than the global calibration data set (Balco et al., 2009).

## 5.4 *Dipstick Creation*

Once exposure ages and uncertainties have been calculated for all samples in a dipstick, Monte Carlo simulations are performed to quantify plausible thinning rates and their associated confidence interval. In each simulation, the samples in the dipstick assume a random age within their internal uncertainty (assuming a normal probability distribution in the uncertainty) and a linear regression is run using the resulting points, producing a unique dipstick each time. 1000 total dipsticks are created for each simulation using MATLAB, with a filter written in to ensure that negative slopes (indicating thickening through time) are discarded. The 1000 unique dipsticks are used to quantify the mean thinning rate (given by the average slope of the dipsticks), its 90% confidence interval, and time of thinning (given by its location on the x-axis). Because Monte Carlo simulations in this project are performed using vertically-separated data with x-axis (age) uncertainties and no y-axis (elevation) uncertainties, and negative slopes are discarded, it is expected that probability distributions of the dipstick thinning rates will be right skewed (i.e., the larger the uncertainties, the larger the number of simulations that will feature lower slopes). This distribution reflects the possibility of ice thinning rates far higher than the mean in these simulations, especially if age uncertainties overlap at different elevations.

## 6 RESULTS

### 6.1 *Difficulties in Mineral Separation*

Given the scale of this project, it was inevitable that I would encounter difficulties at some point. As it turned out, isolating quartz from 80 samples took a significantly longer time than expected and was performed incorrectly on some samples during the first attempt at mineral separation. Because of this, at the time of writing, exposure ages have been obtained for only 42 samples in New England (Table 3). While five additional samples have been processed for Mt. Jacques-Cartier in Quebec, the need for more data from this location and its isolation relative to all other samples makes meaningful interpretation of the calculated exposure ages difficult. This thesis instead focuses on the 42 ages calculated in New England. This section will describe where I encountered difficulties and made errors during sample processing, both to explain why the dataset presented here is incomplete and to demonstrate the importance of following tested, established procedures. My hope is that by explaining the difficulties I experienced during this process, others may avoid them in their work.

Extracting quartz from 80 samples requires a substantial amount of time and equipment. Some samples were collected from quartz veins or extrusions, and required little processing, while others were collected from rocks of fine-grained lithologies and required substantial work to isolate their quartz components. While physical separation methods such as magnetic separation (Corbett et al., 2016), density separation, and froth flotation (Somasundaran, 1975), can remove many mineral phases from a sample, they alone are almost never able to completely isolate quartz. As discussed in section 5, complete quartz isolation requires the use of chemical separation methods, specifically the procedure developed by Kohl and Nishiizumi (1992)

involving the use of diluted, inorganic acids to dissolve other mineral phases with minimal quartz loss.

Herein lies the first error of this project. Due to the large number of samples, limited number of sonicators available (2), and limited number of 4-liter jugs that could fit in each sonicator (3), I quickly realized that the Kohl and Nishiizumi (1992) method would take many months to complete. In an effort to speed up the process, more than 50 g of sample were placed in each container, which caused incomplete quartz isolation in many samples. Unfortunately, this did not become apparent until well into the mineral separation process, when a batch of samples was sent to the University of Vermont Cosmogenic Nuclide Lab for quartz purity testing on their ICP-OES and only about 10% were below the threshold for pure quartz.

This discovery led to a re-evaluation of the processing procedure and a return to the strict method developed by Kohl and Nishiizumi (1992). Given that I was scheduled to start chemical extraction of Be at UVM in less than a month, this meant that I would not be able to complete quartz isolation on all samples by the time Be extraction began. Because the Be extraction process takes a week for every 10 samples (Corbett et al., 2016), I planned to finish quartz isolation on the samples that needed more work while beginning Be extraction on the samples that had passed the purity test. Fortunately, the University of Vermont Cosmogenic Nuclide Lab is a tremendous facility dedicated to cosmogenic nuclide extraction and includes a mineral separation lab with 10 sonicators for quartz isolation on a large scale.

To complete quartz isolation on my remaining samples in the few weeks in which I was at the University of Vermont, I decided to put the samples through daily 1% acid etches, instead of moving to weaker, longer etches. This was my second error. Using 1% acid daily not only dissolves a fair amount of quartz, it also produces a substantial number of aqueous cations from

dissolved mineral phases that must be poured off the sample. Although I did daily rinses of the samples, I clearly did an incomplete rinse job on about 30 of them, for those cations (I believe they were  $\text{Al}^+$  and  $\text{K}^+$ , sourced from feldspar minerals) joined  $\text{F}^-$  anions (from the HF being added daily) to form durable fluoride precipitates in these samples. These little white blobs are some of the toughest materials I have ever encountered; and resisted almost every one of my attempts to remove them from my samples.

Leaning on the experience of Dr. Paul Bierman, Professor of Geology at the University of Vermont and director of the Cosmogenic Nuclide Lab, I tried several methods to rid my contaminated samples of these fluoride precipitates. First, I tried heating the samples (at  $95^\circ\text{C}$ ) in 10% perchloric acid, eventually evaporating the acid off the samples. This seemed to have very little effect on the precipitates. Next, I tried heating the samples (at  $95^\circ\text{C}$ ) in 1% HF and 1% HCL overnight, which also had little effect. At this point, I reverted to physical separation methods, experimenting with an adapted density separation method where I attempted to sink the quartz components of each sample while the fluoride precipitates, which seemed to have a lower density, floated. This worked reasonably well on most samples but did not completely rid any samples of the precipitates. Following this, I tried a method described in Connelly et al. (2006), which involved heating the samples (at  $140^\circ\text{C}$ ) in 2 mL of 14M  $\text{HNO}_3$  for 24 hours, then adding 1 mL of 12N HCl and heating until dry. After drying, I added 1 mL of 6N HCl, heated until dry, and then added 1 mL of 0.5M HCl and dried once more. This method, following density separation, worked reasonably well, clearing eight samples of fluoride precipitates and allowing them to pass the UVM quartz purity test.

Ultimately, however, about 33 samples were not able to be chemically processed this year, due both to lingering fluoride precipitate contamination and to the excessive loss of quartz

that some samples experienced during the aggressive acid etches. This was a disappointment, but I have begun re-processing many of these samples and will be extracting Be from 10 of them in August, 2018, with the intention to ultimately re-process all 33. This master's thesis, therefore, serves as an intermediate report on this multi-year project, which I will finish during my Ph.D., showing the data that we currently have and the preliminary conclusions we can draw from it.

## **6.2 *Calculated Exposure Ages and Dipsticks***

An unfortunate reality of the fluoride precipitate contamination is that it did not affect samples from just one or two locations, but from every site we sampled. Therefore, many of the sample locations have incomplete dipsticks, and I must wait for more data before dipsticks can be confidently constructed. Note, in the following sections, any uncertainty presented with an exposure age will be the  $1\sigma$  internal uncertainty.

### **6.2.1 Peekamoose Mt., Catskills, NY**

The five processed exposure ages from Peekamoose Mt. are split into two distinct groups that do not overlap when uncertainty is included. Higher elevation ages range from 19.8-18.6 ka, while lower elevation samples have ages between 17.2-18.5 ka (Table 4).

Monte Carlo dipstick simulations (Fig. 13a) give a 90% confidence interval (5<sup>th</sup> – 95<sup>th</sup> percentiles) for the LIS thinning rate in the Catskills of 0.09 – 0.22 m yr<sup>-1</sup>, with a right-skewed distribution that allows for the possibility of much higher thinning rates. In addition, the highest elevation simulated, 1170 m asl, was first exposed at  $19.46 \pm 0.41$  ka (Fig. 13b).

### **6.2.2 Wachusett Mountain**

Currently, only one surface exposure age has been calculated for Wachusett Mountain (Table 4), giving a date for ice thinning below 369 m asl of  $15.54 \pm 0.76$  ka. The other three

Wachusett samples are currently being processed, so more information about this location should be available in the next year.

### **6.2.3 Mt. Greylock**

Four exposure ages have been calculated on Mt. Greylock (Table 4, Fig. 14a). One of the samples, MG-01, contains more than double the internal uncertainty of any other Greylock sample. This is likely due to the abundance of  $K^+$  and  $Mg^{2+}$  observed in the sample, which was present even after Be extraction and may have caused slight interferences in AMS ratio measurements. Including uncertainty, all ages from Mt. Greylock fall between 13-15.5 ka.

Because of the sample with wide uncertainty, and the low sample total, an initial attempt to perform a Monte Carlo dipstick simulation ensemble produced poorly-constrained statistics (Fig. 14b). The 90% confidence interval for simulated thinning rates at Mt. Greylock is  $0.06 - 0.41 \text{ m yr}^{-1}$  (Fig. 14b), while highest simulated exposure (1060 m asl) occurred at  $14.88 \pm 1.16$  ka (Fig. 14c).

### **6.2.4 Killington Mountain**

All but two of the Killington samples (KM-01 and -02) have been processed and have had exposure ages calculated (Table 4). Samples from boulders at 1041 and 919 m asl produced exposure ages of 10.9 and 9.8 ka, respectively, considerably post-dating LIS retreat as given by existing glacial chronologies in the region (Fig. 8; Dyke, 2004; Ridge et al., 2012). Exposure ages from summit bedrock samples are indistinguishable within uncertainty from a boulder sample located more than 500 m below the summit (all ages between 14.6-15 ka; Table 4). One of two basal samples produced an exposure age predating all other samples ( $19.2 \pm 1.1$  ka), an age that is distinctly different than that of a sample located only 6 m higher ( $12.9 \pm 0.7$  ka; Table 4).

With three out of seven samples producing suspect exposure ages, it will be difficult to create a thinning history here with confidence. However, the four other data points give a thinning rate 90% confidence interval of 0.10 – 0.41 m/yr (Fig. 15b) and suggest that the Killington summit (1288 m asl) was exposed at  $14.99 \pm 0.28$  ka (Fig. 15c).

### **6.2.5 Jay Peak**

Seven exposure ages have been calculated for samples on Jay Peak (Fig. 16; Table 4). Two bedrock samples from the summit of Jay Peak (1174 m asl) have overlapping exposure ages of  $13.6 \pm 0.4$  and  $14.2 \pm 0.4$  ka, while another is slightly older at  $16.2 \pm 0.5$  ka. A lower-elevation (831 m asl) boulder has an exposure age similar to the older summit sample, while a bedrock sample from 1084 m asl and a boulder sample from 712 m asl produced younger exposure ages of  $11.4 \pm 0.4$  and  $11.5 \pm 0.4$  ka, respectively. A boulder resting on a gentle slope about 100 m below the summit has an exposure age of  $5.0 \pm 0.4$  ka, postdating ice recession from the area by almost 8 kyr (Fig. 8). The scatter in the exposure ages and limited number of samples makes confidence in results from Jay Peak minimal at this stage, and the construction of a dipstick will wait until more data is collected.

### **6.2.6 Mt. Bigelow**

During sample processing, it became apparent that quartz from the Bigelow samples contained unusually large amounts of Al in its structure. After repeated rounds of acid etching, and microscope analysis to determine that the sample had been reduced to almost pure quartz, the samples from Bigelow continued to register Al concentrations of 500-1000 ppm on the ICP-OES (the standard for “pure” quartz is <200 ppm Al). This realization meant that to process the Bigelow samples, the Be extraction procedure followed at the University of Vermont Cosmogenic Nuclide Lab (Corbett et al., 2016) had to be modified. Before running the samples

through cation column chromatography, in which the cations in the sample are separated, each Bigelow sample was split into equal aliquots which were run separately. This method worked well on three of the samples (BP-02, -03, and -06), but sample BP-05 still contained so much Al that it overloaded its columns, failing to separate the cations. This sample had to be discarded.

In total, only three samples have been fully processed for Mt. Bigelow, a boulder-bedrock pair at the summit (BP-02 and -03) and a boulder at the base (BP-06; Table 4). The summit bedrock has an exposure age of  $27.3 \pm 0.7$  ka, approximately a thousand years older than the onset of the LGM, while the adjacent boulder yielded an exposure age almost ten thousand years younger ( $17.8 \pm 0.5$  ka). The sample at the base has a considerably younger exposure age of  $14.1 \pm 0.6$  ka.

### **6.2.7 Franconia Notch**

In total, 11 samples from Franconia Notch have had exposure ages calculated, covering a wide range of elevations (Fig. 17 & 18). Four high-elevation samples (>1400 m asl) had exposure ages older than the LGM, ranging from  $23.7 \pm 0.6$  to  $151.2 \pm 1.6$  ka (Table 4). One boulder sample from mid-elevations (1087 m asl) had an exposure age of  $10.0 \pm 0.5$  ka, post-dating ice-recession from New England. Because these ages probably do not correspond to exposure due to the LIS thinning, they are not included in Monte Carlo dipstick simulations.

The remaining seven samples from Franconia Notch are believed to have exposure ages corresponding to the LIS lowering below their elevation. A Mt. Lafayette bedrock sample from 1354 m asl has a similar exposure age ( $12.9 \pm 0.5$  ka) as boulders from the slope of Mt. Lafayette (711 m asl,  $12.7 \pm 0.5$  ka), a bluff above the valley floor (662 m asl,  $13.2 \pm 0.4$  and  $13.1 \pm 0.6$  ka) and the valley floor (624 m asl,  $12.3 \pm 0.4$  ka). The only older age comes from a boulder at 1251 m asl ( $14.6 \pm 0.4$  ka). Monte Carlo dipstick simulations using these samples (Fig. 19a) give an

ice thinning rate 90% confidence interval of 0.05 – 0.35 m/yr with a right-skewed probability distribution (Fig. 19b) and indicate that ice had lowered to 1354 m asl by  $13.73 \pm 0.35$  ka (Fig. 19c).

### **6.2.8 Mt. Mansfield**

Mt. Mansfield exposure ages collected and processed by myself (Table 4) and Lee Corbett, Paul Bierman, P. Thompson Davis, Jeremy Shakun, and Alexandria Koester (Table 5) are considered together in this section. One of the summit samples (1300 m asl) had an age older than the LGM, and three other samples above 1200 m asl had ages between 16.9-18.9 ka, not overlapping any lower ages within  $2\sigma$  uncertainty (Fig. 20). A cluster of eight bedrock and boulder samples between 1150-1200 m asl produced similar ages, all roughly between 14-15 ka (Table 5; Fig. 20). The ages from three bedrock samples located between 900 – 1100 m asl and two basal boulder samples (~410 m asl) share a similar age range, overlapping between around 13.5-14.5 ka.

Two boulder samples from mid-elevations (923 and 826 m asl) produced similar, younger exposure ages of  $12.6 \pm 0.5$  and  $12.6 \pm 0.4$  ka, respectively, that overlap with one of the basal boulders within  $1\sigma$  uncertainty. When  $2\sigma$  uncertainty is considered, the young mid-elevation boulders overlap in age with both basal boulders and four of the mid-elevation samples. Although these samples are younger than expected given their location, their identical ages and overlap of other ages within  $2\sigma$  uncertainty adds confidence to their validity. To analyze the effect of including vs. excluding these ages, Monte Carlo dipstick simulations were run for both cases (Fig. 21b). Removing the young boulder ages shifted the distribution of simulated thinning rates towards faster rates (from 0.08-0.22 to 0.10-0.36 m yr<sup>-1</sup> 90% confidence intervals).

### 7.1 *Interpretation of exposure age outliers*

Sixteen exposure ages produced during this project (including the Mansfield samples collected before my involvement) do not appear to correspond to the timing of LIS retreat and require further consideration to explain their anomalous exposure ages.

#### 7.1.1 **Anomalously Old, Pre-LGM Exposure Ages**

Some exposure ages appear too old to represent deglacial thinning based on the existing southeastern LIS retreat chronology (Fig. 8). Because all the high elevation samples from Franconia Notch had exposure ages older than the LGM (Fig. 18), their ages are unlikely to represent early exposure during the initial LIS deglaciation. It is more likely that the erosional power of ice at these elevations was weaker than at lower elevations, resulting in incomplete removal of inherited  $^{10}\text{Be}$  from previous exposures. The same conclusion was reached by Bierman et al. (2015) for high-elevation samples from Mt. Washington and Little Haystack, New Hampshire, and Mt. Katahdin, Maine. Bierman et al. hypothesized that pre-LGM exposure ages could result from two mechanisms, incomplete removal of surficial bedrock by non-erosive ice or incomplete coverage of these summits by a thinner LIS. To test these hypotheses, Bierman et al. measured the concentration of *in-situ*  $^{14}\text{C}$  in several samples.  $^{14}\text{C}$  has a half-life of about 5730 years, so if the LIS covered these summits for 30 kyr, approximately five half-lives of  $^{14}\text{C}$ , there would be virtually no inherited  $^{14}\text{C}$  left in the bedrock. Every  $^{14}\text{C}$  exposure age calculated by Bierman et al. was younger than 13 ka, indicating that ice did cover the summits, but did not erode sufficient material to remove inherited  $^{10}\text{Be}$ .

All but one high-elevation sample from Mt. Mansfield produced exposure ages younger than the LGM, but still inconsistent with the age-elevation trend of lower-elevation samples (Fig. 20), making the interpretation of ages for this mountain more complicated than at Franconia Notch. The pattern of ages from Mt. Mansfield could indicate two possible thinning histories: (1) ice thinned at a continuous rate for the duration of its retreat around Mt. Mansfield, but ice at higher elevations eroded less vigorously than ice at lower elevations and failed to remove all the inherited cosmogenic nuclides from the bedrock; (2) ice eroded all inherited cosmogenic nuclides from bedrock at all elevations, but thinned slowly from  $\sim 18.5 - 14.5$  ka, exposing the higher elevations of Mt. Mansfield, before thinning accelerated from  $\sim 14.5 - 13$  ka lower on the mountain. The evidence for cold-based ice at high elevations in the White Mountains and Mt. Katahdin (Bierman et al., 2015) may provide some support for the former scenario.

One more interesting case of apparent  $^{10}\text{Be}$  inheritance was found at Mt. Bigelow. While the summit bedrock sample has an exposure age of  $27.3 \pm 0.7$  ka, preceding the LGM, a nearby boulder sample has an exposure age of  $17.8 \pm 0.5$  ka. Notably, the boulder was composed of the local lithology and looked as if it may have been plucked from bedrock nearby, providing little opportunity for its surface to have been eroded along the way. Why, then, does the boulder sample seem to have experienced sufficient erosion to have removed most, if not all, of the inherited  $^{10}\text{Be}$  from previous exposures, while the nearby bedrock seems to contain those inherited  $^{10}\text{Be}$  atoms? One possibility is that the boulder may have been turned over during transport, exposing a surface to cosmic rays that had not previously been exposed.

### **7.1.2 Anomalously young, Holocene exposure ages**

Other samples from this project produced exposure ages that appear anomalously young in comparison to the existing retreat chronology of the LIS (Fig. 8; e.g. Balco et al., 2002; Ridge

et al., 2012; Bromley et al., 2015; Thompson et al., 2017). These ages all come from boulders. Examples include a boulder from 1060 m asl on Jay Peak (5.0 ka; Fig. 16), 1087 m asl in Franconia Notch (10.0 ka; Fig. 18)), and two boulders from 1041 and 919 m asl on Killington Mt. (10.9 and 9.8 ka respectively; Fig. 15). While not located in valley bottoms, all of these samples were located below slopes of 10-20°. With the exception of the 5.0 ka Jay Peak boulder, the exposure ages of these boulders post-date deglaciation by only a few thousand years, possibly reflecting post-glacial landscape stabilization.

### **7.1.3 Anomalous deglacial exposure ages**

A final subset of anomalous exposure ages date to the last deglaciation but seem difficult to reconcile with other ages in a given dipstick or prior chronologies of ice margin retreat. One example is a basal (593 m asl) boulder sample from Killington Mt. with an exposure age of  $19.1 \pm 1.1$  ka (KM-09; Fig. 15). Considering the summit (~1288 m asl) samples from Killington, which produced exposure ages of  $14.6 \pm 0.4$  (KM-03) and  $15.1 \pm 0.4$  ka (KM-04; Fig. 15), and previously-published constraints on the retreat of the southeastern LIS, which suggest that the ice margin was still located to the south of Killington at around 15 ka (Fig. 5; Ridge et al., 2012), it seems highly unlikely that a boulder at the base of Killington was exposed around 19 ka. This exposure age may instead reflect the presence of inherited  $^{10}\text{Be}$  in the sample.

Another example of a marginally-anomalous exposure age was observed at Jay Peak. Despite being sampled from nearby quartz veins, one summit sample (JP-03) had an exposure age about 2 kyr older than the other two summit samples ( $16.2 \pm 0.5$  vs.  $14.2 \pm 0.4$  and  $13.6 \pm 0.4$  ka; Fig. 16). Presently, it is not clear which age reflects the true exposure of the Jay Peak summit.

## **7.2 General Trends**

### **7.2.1 Overlapping Exposure Ages**

At most of the mountains selected for this project, exposure ages overlap within internal uncertainty across many elevations. For example, at Franconia Notch, a sample from 1354 m asl has an exposure age ( $12.9 \pm 0.5$  ka) that overlaps the ages of low-elevation samples from 662 m asl ( $13.1 \pm 0.6$  and  $13.2 \pm 0.4$  ka), 624 m asl ( $12.3 \pm 0.4$  ka), and 711 m asl ( $12.7 \pm 0.5$  ka) (Table 3; Fig. 18). A similar pattern can be seen at Mt. Greylock (Table 4; Fig. 14), Killington Mt. (Table 4; Fig. 15), and Mt. Mansfield (Table 4; Fig. 20). This pattern of indistinguishable exposure ages across a substantial vertical range allows for the possibility that ice thinned at rates faster than are captured by Monte Carlo simulations in these locations. If ice thinned at rates of  $>1$  m yr<sup>-1</sup>, the resultant exposure ages across our sampled elevations would be so similar that their differences could not be resolved with the current precision of <sup>10</sup>Be exposure ages.

### **7.2.2 North-South Trend**

In general, exposure ages are younger to the north. The southernmost sampling location, Peekamoose Mt. in the Catskills (41.9°N), produced the earliest exposure ages of this project (not including those suspected of having inherited <sup>10</sup>Be), with ages ranging from 19.5 – 17.7 ka (Table 4). Mt. Greylock (42.6°N), Wachusett Mt. (42.5°N), and Killington Mt. (43.6°N) show evidence of LIS thinning between around 15.5-14 ka, with thinning continuing down Killington until ~13 ka (Table 4; Fig. 15). Farther north, Mt. Mansfield (44.5°N) and Franconia Notch (44.2°N) predominately show evidence of ice thinning between 14-13 ka.

## **7.3 Timing of southeastern LIS thinning**

### **7.3.1 Early Heinrich Stadial 1 (19.5-17.5 ka) Thinning**

The earliest exposure of any sample site is observed in the Catskill Mountains of southern NY, where three samples from the summit of Peekamoose Mt. agree within internal uncertainty on exposure around 19.5 ka (Table 4; Fig. 13). Furthermore, all samples from Peekamoose Mt. are between ~19.5-17.5 ka, suggesting ~900 m of LIS thinning during early HS1 (Fig. 5; McManus et al., 2004; Ritz et al., 2013). This thinning, combined with varve evidence for southeastern LIS retreat from coastal Connecticut to southern Massachusetts (Fig. 8; Ridge et al., 2012), suggests substantial ice loss from the southeastern LIS during early HS1.

The timing of this ice loss supports the arguments of Thornalley et al. (2010), Carlson and Clark (2012), and Alvarez-Solas et al. (2013), that LIS meltwater, rather than the Heinrich Event 1 iceberg discharge event, caused NADW formation to slow at the beginning of HS1. In this case, it was likely the subsurface warming resulting from reduced convection that triggered Heinrich Event 1 (Alvarez-Solas et al., 2013). While Stokes (2017) pointed out that there was no significant retreat on most LIS margins prior to the HS1 AMOC slowdown, the Catskills dipstick provides preliminary evidence that the southeastern LIS was thinning from approximately 19.5-17.5 ka, supporting the argument that there was a substantial meltwater flux coming from at least this sector.

### **7.3.2 Late Heinrich Stadial 1 (~17.6 – 14.6 ka) Thinning**

Summit exposure ages from several mountains indicate that the LIS was continuing to thin from 17.6-14.6 ka, but there are few data points to constrain the timing or rate of thinning. The highest exposure age from Mt. Greylock indicates that ice had lowered to 1060 m asl in northwestern Massachusetts by  $15.7 \pm 0.4$  ka, with dipstick simulations suggesting thinning around Mt. Greylock until  $13.9 \pm 0.4$  ka (Fig. 14), straddling the transition from HS1 to the B-A (Clark et al., 2012). A single exposure age from Wachusett Mountain suggests that the LIS

surface had lowered to 369 m asl in central Massachusetts by  $15.5 \pm 0.8$  ka (Table 4). Further north, two samples from the summit of Killington Mountain (1288 m asl) in central Vermont constrain its initial exposure from under the LIS to  $15.0 \pm 0.3$  ka (Table 4; Fig. 15). It should be noted that the accuracy of LIS thinning histories simulated at each of these locations should be treated with caution at this time due to the limited number of data points believed to correspond to LIS ice thinning ( $n = 4$  at Greylock,  $n = 1$  at Wachusett,  $n = 4$  at Killington).

The idea of continued southeastern LIS thinning through late HS1 is consistent with observations from Davis et al. (2015) and Koester et al. (2017) suggesting rapid thinning in central and coastal Maine, respectively, during this time. The exposure of peaks in Massachusetts and central Vermont suggest that this thinning was not limited to Maine.

### 7.3.3 Bølling-Allerød (~14.6 – 12.9 ka) Thinning

Ice-extent indicators in northern New England (e.g. Spear et al., 1994; Dyke, 2004; Ridge et al., 2012; Bromley et al., 2015; Thompson et al., 2017) show that southeastern LIS retreat accelerated dramatically following the transition into the B-A. Initial  $^{10}\text{Be}$  exposure ages from Mt. Washington, NH, indicate that the southeastern LIS also thinned rapidly during the transition into the B-A, with indistinguishable exposure ages ( $n = 5$ ) between 1400 – 700 m asl centered on  $14.3 \pm 0.4$  ka (Koester et al., *in prep.*).

The exposure ages and dipsticks produced to date in this project largely agree with the data from Mt. Washington in Koester et al. (*in prep.*), indicating substantial southeastern LIS thinning during the B-A. While the initial exposures of Killington Mt. and Mt. Greylock seem to have occurred late in HS1, exposure ages from lower elevations on both mountains date to the B-A, indicating thinning through the B-A transition (Table 4; Fig. 14 & 15). Samples from 1200 m asl on Mt. Mansfield and 1354 m asl on Mt. Lafayette were first exposed following the transition

into the B-A (Fig 17c & 20c; Table 4), and the thinning at each location occurred entirely within the B-A. The loss of ~800 m of ice thickness at both these locations indicates that the southeastern LIS lost a substantial volume of ice during the B-A.

#### **7.4 Rate of southeastern LIS thinning**

The uncertainty associated with  $^{10}\text{Be}$  exposure ages and the limited number of samples currently processed at most of our dipstick locations prevent confident statements about the southeastern LIS thinning rate beyond order-of-magnitude statements. At the moment, the Catskills dipstick is the only available constraint on southeastern LIS pre-HS1 thinning. Monte Carlo simulations suggest that thinning rates mostly fall between  $0.09 - 0.22 \text{ m yr}^{-1}$  (Fig. 13b), suggesting millennial-scale thinning but not eliminating the possibility of century-scale thinning at far higher rates.

The exposure ages calculated for this project support the conclusion of Koester et al. (*in prep*) that the LIS thinned rapidly during or shortly following the transition into the B-A. The initial exposure of Killington Mt. occurred shortly before MWP-1A, and while the Killington dipstick has large uncertainties at the moment due to the small sample size, Monte Carlo simulations display thinning rates between  $0.10 - 0.41 \text{ m yr}^{-1}$  during the B-A. Further north, a similar range of thinning rates is seen in Franconia Notch and Mt. Mansfield, although the thinning at both locations appears to have occurred entirely during the B-A (Table 4; Fig. 19 & 21). The thinning at Mt. Mansfield slightly pre-dates the thinning at Franconia Notch, but Monte Carlo dipstick simulations have them overlapping between approximately 14-13 ka. The similar 90% confidence intervals for simulated thinning rates at Franconia Notch ( $0.10 - 0.41 \text{ m yr}^{-1}$ )

and Mt. Mansfield ( $0.08 - 0.22$  or  $0.10 - 0.36 \text{ m yr}^{-1}$ ) suggests that regional, rapid ice thinning may have been occurring at this time.

### **7.5 Comparison to Present-Day Thinning Observations in Greenland and Antarctica**

The range of possible southeastern LIS thinning rates observed in the 90% confidence intervals at each dipstick location overlap thinning rates observed in recent years in the Amundsen Sea embayment area of Antarctica ( $0.139 \pm 0.07 \text{ m yr}^{-1}$ ) and in slow-flowing regions of Greenland ( $0.12 \text{ m yr}^{-1}$ ). However, even at the high end of the thinning rate 90% confidence intervals ( $\sim 0.4 \text{ m yr}^{-1}$ ), southeastern LIS thinning during the B-A is about half the rate observed in fast-flowing regions of Greenland ( $0.84 \text{ m yr}^{-1}$ ) and an order of magnitude slower than dynamic thinning observed in some Antarctic outlet glaciers ( $4 - 9 \text{ m yr}^{-1}$ ; Pritchard et al., 2009). It should be noted, though, that these fast thinning rates in Greenland and Antarctica are from only a few small, exceptionally fast-flowing ice streams and do not represent the thinning rates observed over the majority of the ice sheets (Pritchard et al., 2009). Additionally, as mentioned in section 5.4, the 90% confidence intervals for Monte Carlo simulated thinning rates do not capture the distinct possibility of extremely fast thinning ( $>1 \text{ m yr}^{-1}$ ) that could have occurred at many of the sampled locations.

### **7.6 Future Work**

As stated in the 'Results' section, this project is ongoing, and about 33 more samples will have exposure ages calculated in the next year. The expected data will fill in many of the dipsticks presented here, including samples from Franconia, Mansfield, Jay, Wachusett, Peekamoose, Bigelow, and Jacques-Cartier currently being processed. Additionally, eight

samples from Mt. Monadnock, in southern New Hampshire, will be processed in the next year. Due to its location between the more southern dipstick sites (Catskills, Greylock, Wachusett) and the northern sites (Franconia, Mansfield, Jay Peak, Bigelow, Jacques-Cartier), as well as its isolation from other topographic features (it is the namesake for a ‘monadnock’, or a stand-alone mountain), the Mt. Monadnock dipstick is expected to provide valuable information on the thinning behavior of the southeastern LIS during its deglaciation.

Ultimately, these data will be merged with the dipsticks from Davis et al. (2015) and Koester et al. (2017, *in prep*) as well as all other southeastern LIS retreat chronologies (Fig. 8) and combined statistically to produce a series of probabilistic 3D ice sheet reconstructions for the last deglaciation. These reconstructions will not only offer an unparalleled view of ice sheet retreat behavior, but will be useful for LIS volume estimates, sea level contributions, and analysis of the interactions between the retreating LIS and other elements of the climate system.

## 8 CONCLUSION

Ice sheet orography remains one of the largest unknowns in reconstructions of the deglacial paleoclimate, inhibiting a greater understanding of ice sheet decay dynamics and their interactions with global climate. Chronometric ‘dipsticks’ composed of cosmogenic nuclide exposure ages along vertical transects offer a potential solution to this problem, as they allow for the lowering paleo-ice surface to be tracked as it exposed more and more landmass in areas of high topographic relief. This project set out to calculate 80  $^{10}\text{Be}$  ages between 10 sample locations that span across New England and southern Quebec to create a series of dipsticks that could be used to determine the timing and rate of southeastern Laurentide Ice Sheet thinning during the last deglacial period. Difficulties were encountered during mineral separation on some of these samples, but 42 samples have had exposure ages calculated at the time this thesis was written.

Despite this setback, the exposure ages that have been calculated provide valuable information. Exposure ages from the Catskill Mountains, NY, record southeastern Laurentide thinning early in the deglacial period (~19.5 ka), prior to the onset of Heinrich Stadial I. This evidence supports arguments that a retreating and thinning Laurentide flooded the North Atlantic with fresh water during the initial stage of deglaciation, slowing overturning circulation and reducing northward oceanic heat transport, causing Heinrich Stadial I. Exposure ages from Franconia Notch, NH, and Mt. Mansfield, VT, support evidence from previously-collected Mt. Washington, NH, exposure ages, that the southeastern Laurentide experienced rapid thinning in northern New England during the Bølling-Allerød warm period.

Conclusive statements about the thinning rates of the southeastern Laurentide are difficult to make at this time, as many dipstick locations currently have insufficient data to construct a confident dipstick. However, the probability distributions for thinning rates at several dipstick locations suggest that southeastern Laurentide thinning probably generally occurred at rates between 0.1-0.8 m yr<sup>-1</sup>, comparable to thinning rates observed today in Greenland and Antarctica. It should be noted that in some locations exposure ages from different elevations overlapped within uncertainty, so while Monte Carlo analyses suggested a population of possible thinning rates mostly below 1 m yr<sup>-1</sup>, much higher thinning rates, on the order of multiple meters per year, cannot be completely discarded.

## References Cited

- Abe-Ouchi, A., Saito, F., Kageyama, M., et al., 2015, Ice-sheet configuration in the CMIP5/PMIP3 Last Glacial Maximum experiments: *Geoscientific Model Development*, v. 8, no. 11, p. 3621-3637.
- Abe-Ouchi, A., Saito, F., Kawamura, K., Raymo, M.E., Okuno, J., Takahashi, K., and Blatter, H., 2013, Insolation-driven 100,000-year glacial cycles and hysteresis of ice-sheet volume: *Nature*, v. 500, no. 7461, p. 190.
- Abe-Ouchi, A., Segawa, T., and Saito, F., 2007, Climatic Conditions for modelling the Northern Hemisphere ice sheets throughout the ice age cycle: *Climate of the Past*, v. 3, no. 3, p. 423-438.
- Ackermann, M., Ajello, M., Allafort, A., et al., 2013, Detection of the Characteristic Pion-Decay Signature in Supernova Remnants: *Science*, v. 339, no. 6121, p. 807-811.
- Ackert, R.P., Jr, Mukhopadhyay, S., Parizek, B.R., and Borns, H.W., 2007, Ice elevation near the West Antarctic Ice Sheet divide during the Last Glaciation: *Geophysical Research Letters*, v. 34, no. 21, p. L21506.
- Alley, R.B., 2007, Wally Was Right: Predictive Ability of the North Atlantic "Conveyor Belt" Hypothesis for Abrupt Climate Change: *Annual Review of Earth and Planetary Sciences*, v. 35, p. 241.
- Alvarez-Solas, J., Robinson, A., Montoya, M., and Ritz, C., 2013, Iceberg discharges of the last glacial period driven by oceanic circulation changes: *Proceedings of the National Academy of Sciences of the United States of America*, v. 110, no. 41, p. 16350-16354.
- Applegate, P.J., Kirchner, N., Stone, E.J., Keller, K., and Greve, R., 2012, An assessment of key model parametric uncertainties in projections of Greenland Ice Sheet behavior: *The Cryosphere*, v. 6, no. 3, p. 589-606.
- Archer, D., Eby, M., Brovkin, V., et al., 2009, Atmospheric Lifetime of Fossil Fuel Carbon Dioxide: *Annual Review of Earth and Planetary Sciences*, v. 37, no. 1, p. 117-134.
- Arzel, O., England, M.H., and Sijp, W.P., 2008, Reduced Stability of the Atlantic Meridional Overturning Circulation due to Wind Stress Feedback during Glacial Times: *Journal of Climate*, v. 21, no. 23, p. 6260-6282.
- Balco, G., 2011, Contributions and unrealized potential contributions of cosmogenic-nuclide exposure dating to glacier chronology, 1990-2010: *Quaternary Science Reviews*, v. 30, no. 1-2, p. 3-27.
- Balco, G., Briner, J., Finkel, R.C., Rayburn, J.A., Ridge, J.C., and Schaefer, J.M., 2009, Regional beryllium-10 production rate calibration for late-glacial northeastern North America: *Quaternary Geochronology*, v. 4, no. 2, p. 93-107.
- Balco, G., 2006, Converting Al and Be isotope ratio measurements to nuclide concentrations in quartz: University of Washington Cosmogenic Nuclide Lab internal publication. Retrieved from: [http://hess.ess.washington.edu/math/docs/common/ams\\_data\\_reduction.pdf](http://hess.ess.washington.edu/math/docs/common/ams_data_reduction.pdf)
- Balco, G., Stone, J.O.H., Porter, S.C., and Caffee, M.W., 2002, Cosmogenic-nuclide ages for New England coastal moraines, Martha's Vineyard and Cape Cod, Massachusetts, USA: *Quaternary Science Reviews*, v. 21, no. 20, p. 2127-2135.
- Bard, E., Hamelin, B., Delanghe-Sabatier, D., 2010, Deglacial meltwater pulse 1B and Younger Dryas sea levels revisited with boreholes at Tahiti: *Science*, v. 327, no. 5970, p. 1235-1237.

- Bard, E., Rostek, F., Turon, J.L., and Gendreau, S., 2000, Hydrological Impact of Heinrich Events in the Subtropical Northeast Atlantic: *Science*, v. 289, no. 5483, p. 1321-1324.
- Bard, E., Hamelin, B., Fairbanks, R.G., 1990, U-Th ages obtained by mass spectrometry in corals from Barbados: Sea level during the past 130,000 years: *Nature*, v. 346, p. 456-458.
- Barker, S., Diz, P., Hall, I.R., Broecker, W.S., Vautravers, M.J., Pike, J., and Knorr, G., 2009, Interhemispheric Atlantic seesaw response during the last deglaciation: *Nature*, v. 457, no. 7233, p. 1097-1102.
- Barron, E., and Pollard, D., 2002, High-Resolution Climate Simulations of Oxygen Isotope Stage 3 in Europe: *Quaternary Research*, v. 58, no. 3, p. 296-309.
- Bierman, P.R., Davis, P.T., Corbett, L.B., Lifton, N.A., and Finkel, R.C., 2015, Cold-based Laurentide ice covered New England's highest summits during the last glacial maximum: *Geology (Boulder)*, v. 43, no. 12, p. 1059-1062.
- Bierman, P.R., 2007, Cosmogenic glacial dating, 20 years and counting: *Geology*, v. 35, no. 6, p. 575.
- Bierman, P.R., and Dethier, D., 1986, Lake Bascom and the deglaciation of Northwestern Massachusetts: *Northeastern Geology*, v. 8, p. 32-43.
- Brace, W.F., 1953, The geology of the rutland area, Vermont: Vermont Geological Survey, Bulletin no. 6
- Briner, J.P., Miller, G.H., Davis, P.T., Bierman, P.R., and Caffee, M., 2003, Last Glacial Maximum ice sheet dynamics in Arctic Canada inferred from young erratics perched on ancient tors: *Quaternary Science Reviews*, v. 22, no. 5, p. 437-444.
- Broecker, W.S., 2006a, Abrupt climate change revisited: *Global and Planetary Change*, v. 54, no. 3, p. 211-215.
- Broecker, W.S., 2006b, Was the Younger Dryas Triggered by a Flood?: *Science*, v. 312, no. 5777, p. 1146-1148.
- Bromley, G.R.M., Hall, B.L., Thompson, W.B., Kaplan, M.R., Garcia, J.L., and Schaefer, J.M., 2015, Late glacial fluctuations of the Laurentide Ice Sheet in the White Mountains of Maine and New Hampshire, U.S.A: *Quaternary Research*, v. 83, no. 3, p. 522-530.
- Bromwich, D.H., Toracinta, Helin Wei, H., Oglesby, R.J., Fastook, J.L., and Hughes, T.J., 2004, Polar MM5 Simulations of the Winter Climate of the Laurentide Ice Sheet at the LGM: *Journal of Climate*, v. 17, no. 17, p. 3415-3433.
- Buizert, C., Gkinis, V., Severinghaus, J.P., et al., 2014, Greenland temperature response to climate forcing during the last deglaciation: *Science*, v. 345, no. 6201, p. 1177-1180.
- Caesar, L., Rahmstorf, S., Robinson, A., Feulner, G., and Saba, V., 2018, Observed fingerprint of a weakening Atlantic Ocean overturning circulation: *Nature*, v. 556, p. 191-196.
- Caffee, M.W., Goswami, J.N., Hohenberg, C.M., Marti, K., Reedy, R.C., 1988, Irradiation records in meteorites, in: Kerridge, J.F. (Ed.), *Meteorites and the Early Solar System*: University of Arizona Press, Tucson, p. 205-245.
- Carlson, A.E., and Clark, P.U., 2012, Ice sheet sources of sea level rise and freshwater discharge during the last deglaciation: *Reviews of Geophysics*, v. 50, no. 4.

- Carlson, A.E., Ullman, D.J., Anslow, F.S., He, F., Clark, P.U., Liu, Z., and Otto-Bliesner, B.L., 2012, Modeling the surface mass-balance response of the Laurentide Ice Sheet to Bølling warming and its contribution to Meltwater Pulse 1A: *Earth and Planetary Science Letters*, v. 315-316, p. 24-29.
- Carlson, A.E., and Winsor, K., 2012, Northern Hemisphere ice-sheet responses to past climate warming: *Nature Geoscience*, v. 5, no. 9, p. 607.
- Christman, R.A., 1956, The geology of Mount Mansfield State Forest: Vermont Dept. Forest and Parks, Vermont Development Comm. and Vermont Geological Survey.
- Clark, P.U., Shakun, J.D., Marcott, S.A., et al., 2016, Consequences of twenty-first-century policy for multi-millennial climate and sea-level change: *Nature Climate Change*, v. 6, no. 4, p. 360-369.
- Clark, P.U., and Tarasov, L., 2014, Closing the sea level budget at the Last Glacial Maximum: *Proceedings of the National Academy of Sciences of the United States of America*, v. 111, no. 45, p. 15861-15862.
- Clark, P.U., Shakun, J.D., Baker, P.A., et al., 2012, Global climate evolution during the last deglaciation: *Proceedings of the National Academy of Sciences*, v. 109, no. 19, p. E1134.
- Clark, P.U., Dyke, A.S., Shakun, J.D., et al., 2009, The Last Glacial Maximum: *Science*, v. 325, no. 5941, p. 710-714.
- Clark, P.U., McCabe, A.M., Mix, A.C., and Weaver, A.J., 2004, Rapid Rise of Sea Level 19,000 Years Ago and Its Global Implications: *Science*, v. 304, no. 5674, p. 1141-1144.
- Clark, P.U., Mitrovica, J.X., Milne, G.A., and Tamisiea, M.E., 2002, Sea-Level Fingerprinting as a Direct Test for the Source of Global Meltwater Pulse IA: *Science*, v. 295, no. 5564, p. 2438-2441.
- Clark, P.U., and Mix, A.C., 2002, Ice sheets and sea level of the Last Glacial Maximum: *Quaternary Science Reviews*, v. 21, no. 1, p. 1-7.
- Clark, P.U., Marshall, S.J., Clarke, G.K.C., Hostetler, S.W., Licciardi, J.M., and Teller, J.T., 2001, Freshwater Forcing of Abrupt Climate Change During the Last Glaciation: *Science*, v. 293, no. 5528, p. 283-287.
- Condron, A., and Winsor, P., 2012, Meltwater routing and the Younger Dryas: *Proceedings of the National Academy of Sciences*, v. 109, no. 49, p. 19928-19933.
- Connelly, J.N., Ulfbeck, D.G., Thrane, K., Bizzarro, M., and Housh, T., 2006, A method for purifying Lu and Hf for analyses by MC-ICP-MS using TODGA resin: *Chemical Geology*, v. 233, no. 1, p. 126-136.
- Corbett, L.B., Bierman, P.R., Stone, B.D., Caffee, M.W., and Larsen, P.L., 2017, Cosmogenic nuclide age estimate for Laurentide Ice Sheet recession from the terminal moraine, New Jersey, USA, and constraints on latest Pleistocene ice sheet history: *Quaternary Research*, v. 87, no. 3, p. 482.
- Corbett, L.B., Bierman, P.R., and Rood, D.H., 2016, An approach for optimizing in situ cosmogenic  $^{10}\text{Be}$  sample preparation: *Quaternary Geochronology*, v. 33, p. 24-34.
- Corbett, L.B., Young, N.E., Bierman, P.R., Briner, J.P., Neumann, T.A., Rood, D.H., and Graly, J.A., 2011, Paired bedrock and boulder  $^{10}\text{Be}$  concentrations resulting from early Holocene ice retreat near Jakobshavn Isfjord, western Greenland: *Quaternary Science Reviews*, v. 30, no. 13-14, p. 1739.

- Cuffey, K.M., and Clow, G.D., 1997, Temperature, accumulation, and ice sheet elevation in central Greenland through the last deglacial transition: *Journal of Geophysical Research: Oceans*, v. 102, no. C12, p. 26383-26396.
- Dahl-Jensen, D., Steffensen, J.P., Jouzel, J., et al., 1993, Evidence for general instability of past climate from a 250-kyr ice-core record: *Nature*, v. 364, no. 6434, p. 218-220.
- Davis, P.T., and Davis, R.B., 1980, Interpretation of minimum-limiting radiocarbon dates for deglaciation of Mount Katahdin area, Maine: *Geology*, v. 8, no. 8, p. 396.
- Davis, P.T., Bierman, P.R., Corbett, L.B., and Finkel, R.C., 2015, Cosmogenic exposure age evidence for rapid Laurentide deglaciation of the Katahdin area, west-central Maine, USA, 16 to 15 ka: *Quaternary Science Reviews*, v. 116, p. 95-105.
- Davis, P.T., Koester, A.J., Shakun, J.D., Bierman, P.R., and Corbett, L.B., 2017. Applying the Cosmogenic Nuclide Dipstick Model for Deglaciation of Mt. Washington in Johnson, B., and Eusden, J.D., ed., *Guidebook for Field Trips in Western Maine and Northern New Hampshire: New England Intercollegiate Geological Conference*, Bates College, p. 247-272.  
<https://doi.org/10.26780/2017.001.0014>
- Davis, R., and Schaeffer, O., 1955, Chlorine-36 in nature: *Annals of the New York Academy of Sciences*, v. 62, no. 1, p. 107-121.
- DeConto, R.M., and Pollard, D., 2016, Contribution of Antarctica to past and future sea-level rise: *Nature*, v. 531, no. 7596, p. 591.
- Denton, G.H., Anderson, R.F., Toggweiler, J.R., Edwards, R.L., Schaefer, J.M., and Putnam, A.E., 2010, The Last Glacial Termination: *Science (Washington)*, v. 328, no. 5986, p. 1650.
- Deschamps, P., Durand, N., Bard, E., et al., 2012, Ice-sheet collapse and sea-level rise at the Bølling warming 14,600 years ago: *Nature*, v. 483, no. 7391, p. 559-564.
- Doolan, B., 2017, Compilation bedrock geologic map of the Jay Peak 7.5 minute quadrangle, Vermont: Vermont Geological Survey Open File Report VG99-1, Compiled from Schoonmaker, 1998, and Cady et al., 1963.
- Dunai, T., 2010, *Cosmogenic Nuclides: Principles, Concepts and Applications in the Earth Surface Sciences*. Cambridge University Press, Cambridge, UK.
- Dyke, A.S., and Gibbard, P.L., 2004, *An outline of North American deglaciation with emphasis on central and northern Canada*, Elsevier.
- Eby, M., Zickfeld, K., Montenegro, A., Archer, D., Meissner, K.J., and Weaver, A.J., 2009, Lifetime of Anthropogenic Climate Change: Millennial Time Scales of Potential CO<sub>2</sub> and Surface Temperature Perturbations: *Journal of Climate*, v. 22, no. 10, p. 2501.
- Fairbanks, R.G., 1989, A 17,000 year glacio-eustatic sea level record: Influence of glacial melting rates on the Younger Dryas event and deep-ocean circulation: *Nature*, v. 342, p. 637-642.
- Friedlingstein, P., Solomon, S., Plattner, G.K., Knutti, R., Ciais, P., and Raupach, M.R., 2011, Long-term climate implications of twenty-first century options for carbon dioxide emission mitigation: *Nature Climate Change*, v. 1, no. 9, p. 457.

- Goehring, B.M., Brook, E.J., Linge, H., Raisbeck, G.M., and Yiou, F., 2008, Beryllium-10 exposure ages of erratic boulders in southern Norway and implications for the history of the Fennoscandian Ice Sheet: *Quaternary Science Reviews*, v. 27, no. 3, p. 320-336.
- Gosse, J.C., and Phillips, F.M., 2001, Terrestrial in situ cosmogenic nuclides: theory and application: *Quaternary Science Reviews*, v. 20, no. 14, p. 1475-1560.
- Gregoire, L.J., Payne, A.J., and Valdes, P.J., 2012, Deglacial rapid sea level rises caused by ice-sheet saddle collapses: *Nature*, v. 487, no. 7406, p. 219-222.
- Greve, R., and Blatter, H., 2009, *Dynamics of Ice Sheets and Glaciers*: Berlin, Heidelberg, Springer-Verlag.
- Grootes, P.M., and Stuiver, M., 1997, Oxygen 18/16 variability in Greenland snow and ice with 10–3- to 105-year time resolution: *Journal of Geophysical Research: Oceans*, v. 102, no. C12, p. 26455-26470.
- Hansen, J., Sato, M., Hearty, P., et al., 2016, Ice melt, sea level rise and superstorms: evidence from paleoclimate data, climate modeling, and modern observations that 2 °C global warming could be dangerous: *Atmospheric Chemistry and Physics*, v. 16, no. 6, p. 3761-3812.
- He, F., Shakun, J.D., Clark, P.U., Carlson, A.E., Liu, Z., Otto-Bliesner, B.L., and Kutzbach, J.E., 2013, Northern Hemisphere forcing of Southern Hemisphere climate during the last deglaciation: *Nature*, v. 494, no. 7435, p. 81.
- Heinemann, M., Timmermann, A., Elison Timm, O., Saito, F., and Abe-Ouchi, A., 2014, Deglacial ice sheet meltdown: orbital pacemaking and CO<sub>2</sub> effects: *Climate of the Past*, v. 10, no. 4, p. 1567-1579.
- Hellborg, R., and Skog, G., 2008, Accelerator mass spectrometry: *Mass Spectrometry Reviews*, v. 27, no. 5, p. 398-427.
- Johnsen, S.J., Dahl-Jensen, D., Gundestrup, N., et al., 2001, Oxygen isotope and palaeotemperature records from six Greenland ice-core stations: Camp Century, Dye-3, GRIP, GISP2, Renland and NorthGRIP: *Journal of Quaternary Science*, v. 16, no. 4, p. 299-307.
- Johnson, J.S., Bentley, M.J., Smith, J.A., et al., 2014, Rapid Thinning of Pine Island Glacier in the Early Holocene: *Science*, v. 343, no. 6174, p. 999.
- Keigwin, L.D., Klotsko, S., Zhao, N., Reilly, B., Giosan, L., and Driscoll, N.W., 2018, Deglacial floods in the Beaufort Sea preceded Younger Dryas cooling: *Nature Geoscience*, v. 11, p. 599-604.
- Kleman, J., and Applegate, P.J., 2014, Durations and propagation patterns of ice sheet instability events: *Quaternary Science Reviews*, v. 92, p. 32-39.
- Koester, A.J., Shakun, J.D., Bierman, P.R., and Davis, P., 2017, Rapid thinning of the Laurentide Ice Sheet in coastal Maine, USA during late Heinrich Stadial 1: *Quaternary Science Reviews*, v. 163, p. 180-192.
- Kohl, C.P., and Nishiizumi, K., 1992, Chemical isolation of quartz for measurement of in-situ -produced cosmogenic nuclides: *Geochimica et Cosmochimica Acta*, v. 56, no. 9, p. 3583-3587.
- Lambeck, K., Rouby, H., Purcell, A., Sun, Y., and Sambridge, M., 2014, Sea level and global ice volumes from the Last Glacial Maximum to the Holocene: *Proceedings of the National Academy of Sciences*, v. 111, no. 43, p. 15296-15303.

- Langen, P., and Vinther, B., 2009, Response in atmospheric circulation and sources of Greenland precipitation to glacial boundary conditions: *Climate Dynamics*, v. 32, no. 7, p. 1035-1054.
- Lemaitre, G., and Vallarta, M.S., 1933, On Compton's latitude effect of cosmic radiation: *Physical Review*, v. 43, no. 2, p. 87-91.
- Leventer, A., Domack, E., Gore, D., et al., 2011, Retreat of the East Antarctic ice sheet during the last glacial termination: *Nature Geoscience*, v. 4, no. 3, p. 195-202.
- Licciardi, J.M., Teller, J.T., and Clark, P.U., 1999, Freshwater Routing by the Laurentide Ice Sheet During the Last Deglaciation: in *Mechanisms of Global Climate Change at Millennial Time Scales: Geophysical Monograph Series*, Clark, P.U., Webb, R.S., and Kelgwin, L.D. (editors), v. 112, pp. 177-201.
- Little, C.M., Oppenheimer, M., Alley, R.B., et al., 2007, Toward a New Generation of Ice Sheet Models: *Eos, Transactions American Geophysical Union*, v. 88, no. 52, p. 578.
- Liu, J., Milne, G.A., Kopp, R.E., Clark, P.U., and Shennan, I., 2016, Sea-level constraints on the amplitude and source distribution of Meltwater Pulse 1A: *Nature Geoscience*, v. 9, no. 2, p. 130.
- Liu, Z., Otto-Bliesner, B.L., He, F., et al., 2009, Transient Simulation of Last Deglaciation with a New Mechanism for Bølling-Allerød Warming: *Science*, v. 325, no. 5938, p. 310-314.
- Lyons, J.B., Bothner, W.A., Moench, R.H., and Thompson, J.B., Jr., 1997, Bedrock geologic map of New Hampshire: U.S. Geological survey, 1 map, cross sections, scale 1:250,000, <http://libarchive.dartmouth.edu/cdm/ref/collection/gsmaps/id/2087>.
- MacAyeal, D.R., 1993, Binge/purge oscillations of the Laurentide Ice Sheet as a cause of the North Atlantic's Heinrich events: *Paleoceanography*, v. 8, no. 6, p. 775-784.
- Mackintosh, A., White, D., Fink, D., Gore, D.B., Pickard, J., and Fanning, P.C., 2007, Exposure ages from mountain dipsticks in Mac. Robertson Land, East Antarctica, indicate little change in ice-sheet thickness since the Last Glacial Maximum: *Geology*, v. 35, no. 6, p. 551.
- Maczuga, D.E., 1981, The petrology and geochemistry of the Fitchburg Plutonic Complex, central Massachusetts: Master's thesis, University of Massachusetts
- Margold, M., Stokes, C.R., Clark, C.D., and Kleman, J., 2015, Ice streams in the Laurentide Ice Sheet: a new mapping inventory: *Journal of Maps*, v. 11, no. 3, p. 380-395.
- Marshall, S.J., and Clarke, G.K.C., 1999, Modeling North American Freshwater Runoff through the Last Glacial Cycle: *Quaternary Research*, v. 52, p. 300-315.
- McManus, J.F., Gherardi, J., Francois, R., Brown-Leger, S., and Keigwin, L.D., 2004, Collapse and rapid resumption of Atlantic meridional circulation linked to deglacial climate changes: *Nature*, v. 428, no. 6985, p. 834-837.
- Nick, F.M., Vieli, A., Andersen, M.L., et al., 2013, Future sea-level rise from Greenland's main outlet glaciers in a warming climate: *Nature*, v. 497, no. 7448, p. 235.
- Nishiizumi, K., Kohl, C.P., Arnold, J.R., Klein, J., Fink, D., and Middleton, R., 1991, Cosmic ray produced  $^{10}\text{Be}$  and  $^{26}\text{Al}$  in Antarctic rocks: exposure and erosion history: *Earth and Planetary Science Letters*, v. 104, no. 2, p. 440-454.
- Obbink, E.A., Carlson, A.E., and Klinkhammer, G.P., 2010, Eastern North American freshwater discharge during the Bolling-Allerød warm periods: *Geology*, v. 38, no. 2, p. 171-174.

- Osberg, P.H., Hussey, A.M., II, and Boone, G.M., (editors), 1985, Bedrock geologic map of Maine: Maine Geological Survey, 1 plate, correlation chart, tectonic inset map, metamorphic inset map, color geologic map, cross sections, scale 1:500,000, [http://digitalmaine.com/mgs\\_maps/23](http://digitalmaine.com/mgs_maps/23).
- Peltier, W.R., Argus, D.F., and Drummond, R., 2015, Space geodesy constrains ice age terminal deglaciation: The global ICE-6G\_C (VM5a) model: *Journal of Geophysical Research: Solid Earth*, v. 120, no. 1, p. 450-487.
- Peltier, W.R., and Fairbanks, R.G., 2006, Global glacial ice volume and Last Glacial Maximum duration from an extended Barbados sea level record: *Quaternary Science Reviews*, v. 25, p. 3322-3337.
- Peltier, W.R., 2005, On the hemispheric origins of meltwater pulse 1a: *Quaternary Science Reviews*, v. 24, no. 14, p. 1655-1671.
- Peltier, W.R., 2004, Global glacial isostasy and the surface of the ice-age Earth: the ICE-5G (VM2) model and GRACE: *Annu. Rev. Earth Planet. Sci.*, v. 32, p. 111-149.
- Petee, D.M., Broecker, W.S., and Rind, D., 1985, Does the ocean-atmosphere system have more than one stable mode of operation?: *Nature*, v. 315, no. 6014, p. 21-26.
- Phillips, F.M., Leavy, B.D., Jannik, N.O., Elmore, D., and Kubik, P.W., 1986, The Accumulation of Cosmogenic Chlorine-36 in Rocks: a Method for Surface Exposure Dating: *Science*, v. 231, no. 4733, p. 41-43.
- Portenga, E.W., Bierman, P.R., Duncan, C., Corbett, L.B., Kehrwald, N.M., and Rood, D.H., 2015, Erosion rates of the Bhutanese Himalaya determined using in situ-produced <sup>10</sup>Be: *Geomorphology*, v. 233, p. 112-126.
- Pritchard, H.D., Arthern, R.J., Vaughan, D.G., and Edwards, L.A., 2009, Extensive dynamic thinning on the margins of the Greenland and Antarctic ice sheets: *Nature*, v. 461, no. 7266, p. 971-975.
- Rahmstorf, S., 1996, On the freshwater forcing and transport of the Atlantic thermohaline circulation: *Climate Dynamics*, v. 12, no. 12, p. 799-811.
- Ratcliffe, N.M., Potter, D.B., and Stanley, R.S., 1993, Bedrock Geologic Map of the Williamstown and North Adams Quadrangles, Massachusetts and Vermont, and Part of the Cheshire Quadrangle, Massachusetts: US Geological survey.
- Ridge, J.C., Balco, G., Bayless, R.L., et al., 2012, The new North American Varve Chronology: A precise record of southeastern Laurentide Ice Sheet deglaciation and climate, 18.2-12.5 kyr BP, and correlations with Greenland ice core records: *American Journal of Science*, v. 312, no. 7, p. 685-722.
- Rinterknecht, V.R., Clark, P.U., Raisbeck, G.M., et al., 2006, The Last Deglaciation of the Southeastern Sector of the Scandinavian Ice Sheet: *Science*, v. 311, no. 5766, p. 1449-1452.
- Ritz, S.P., Stocker, T.F., Grimalt, J.O., Menviel, L., and Timmermann, A., 2013, Estimated strength of the Atlantic overturning circulation during the last deglaciation: *Nature Geoscience*, v. 6, no. 3, p. 208.
- Robinson, A., Calov, R., and Ganopolski, A., 2012, Multistability and critical thresholds of the Greenland ice sheet: *Nature Climate Change*, v. 2, no. 6, p. 429.
- Rogers, J.N., 2003, Major Holocene debris flows of Franconia Notch (White Mountains, New Hampshire) recorded in Profile Lake: Doctoral dissertation, University of Massachusetts at Amherst.

- Shakun, J.D., Clark, P.U., He, F., et al., 2012, Global warming preceded by increasing carbon dioxide concentrations during the last deglaciation: *Nature*, v. 484, no. 7392, p. 49-54.
- Somasundaran, P., 1975, Separation Using Foaming Techniques: *Separation Science*, v. 10, no. 1, p. 93-109.
- Spear, R.W., 1989, Late-Quaternary History of High-Elevation Vegetation in the White Mountains of New Hampshire: *Ecological Monographs*, v. 59, no. 2, p. 125-151.
- Stocker, T.F., et al. (editors), 2014, *Climate change: the physical science basis : Working Group I contribution to the Fifth assessment report of the Intergovernmental Panel on Climate Change*: New York, Cambridge University Press.
- Stokes, C.R., 2017, Deglaciation of the Laurentide Ice Sheet from the Last Glacial Maximum: *Geographical Research Letters*, v. 43, no. 2, p. 377-428.
- Stokes, C.R., Tarasov, L., Blomdin, R., et al., 2015, On the reconstruction of palaeo-ice sheets: Recent advances and future challenges: *Quaternary Science Reviews*, v. 125, p. 15-49.
- Stone, J.O., Balco, G.A., Sugden, D.E., Caffee, M.W., Sass, L.C., III, Cowdery, S.G., and Siddoway, C., 2003, Holocene Deglaciation of Marie Byrd Land, West Antarctica: *Science*, v. 299, no. 5603, p. 99-102.
- Sugden, D.E., 1978, Glacial Erosion by the Laurentide Ice Sheet: *Journal of Glaciology*, v. 20, no. 83, p. 367-391.
- Tarasov, L., and Peltier, W.R., 2005, Arctic freshwater forcing of the Younger Dryas cold reversal: *Nature*, v. 435, p. 662-665, doi: 10.1038/nature03617.
- Thompson, W.B., Dorion, C.C., Ridge, J.C., Balco, G., Fowler, B.K., and Svendsen, K.M., 2017, Deglaciation and late-glacial climate change in the White Mountains, New Hampshire, USA: *Quaternary Research*, v. 87, no. 1, p. 96-120.
- Thornalley, D.J.R., Oppo, D.W., Ortega, P., et al., 2018, Anomalously weak Labrador Sea convection and Atlantic overturning during the past 150 years: *Nature*, v. 556, 227-230
- Thornalley, D.J.R., Elderfield, H., and McCave, I.N., 2010, Reconstructing North Atlantic deglacial surface hydrography and its link to the Atlantic overturning circulation: *Global and Planetary Change*, v. 79, no. 3, p. 163-175.
- Toscano, M.A., Peltier, W.R., and Drummond, R., 2011, ICE-5G and ICE-6G models of postglacial relative sea-level history applied to the Holocene coral reef record of northeastern St Croix, U.S.V.I.: investigating the influence of rotational feedback on GIA processes at tropical latitudes: *Quaternary Science Reviews*, v. 30, no. 21, p. 3032-3042.
- Ullman, D.J., Carlson, A.E., Anslow, F.S., Legrande, A.N., and Licciardi, J.M., 2015, Laurentide ice-sheet instability during the last deglaciation: *Nature Geoscience*, v. 8, no. 7, p. 534.
- Ullman, D.J., LeGrande, A.N., Carlson, A.E., Anslow, F.S., and Licciardi, J.M., 2014, Assessing the impact of Laurentide Ice Sheet topography on glacial climate: *Climate of the Past*, v. 10, no. 2, p. 487-507.
- Ver Straeten, C.A., 2013, Beneath it all: bedrock geology of the Catskill Mountains and implications of its weathering: *Annals of the New York Academy of Sciences*, v. 1298, no. 1, p. 1-29.

- Vogt, S., Herzog, G.F., Reedy, R.C., 1990, Cosmogenic nuclides in extra-terrestrial materials: Reviews of Geophysics, v. 28, p. 253-275.
- Weaver, A.J., Saenko, O.A., Clark, P.U., and Mitrovica, J.X., 2003, Meltwater Pulse 1A from Antarctica as a Trigger of the Bolling-Allerod Warm Interval: Science, v. 299, no. 5613, p. 1709-1713
- White, D., Zwartz, D., Pollard, D., et al., 2011, Retreat of the East Antarctic ice sheet during the last glacial termination: Nature Geoscience, v. 4, no. 3, p. 195-202.
- Zen, E., Goldsmith, R., Ratcliffe, N.M., Robinson, P., Stanley, R.S., Hatch, N.L., Shride, A.F., Weed, E.G.A., and Wones, D.R., 1983, Bedrock geologic map of Massachusetts: U.S. Geological Survey, downloaded from: [https://ngmdb.usgs.gov/Prodesc/proddesc\\_16357.htm](https://ngmdb.usgs.gov/Prodesc/proddesc_16357.htm)

## Tables

**Table 1:** Acronyms used in this thesis. Many words in this thesis are abbreviated for space and reading efficiency, but these abbreviations can become confusing. This table provides a guide to the abbreviations used throughout this thesis.

Acronym	Meaning	Notes
AMOC	Atlantic Meridional Overturning Circulation	This is the interhemispherical ocean current flowing from the South Atlantic to the high North Atlantic (explained further in Ch. 2)
AMS	Accelerator Mass Spectrometry	
asl	Above sea level	Usually used for elevation measurements. For example: “the sample was collected at 479 m asl”, meaning 479 meters above (present) sea level.
BSI	Boreal Summer Insolation	This is a measure of the amount of incoming solar radiation received at boreal (high Northern) latitudes
ESL	Eustatic Sea Level	The global average sea level at any one time
kyr	Thousand (calendar) years	Ex: 16 kyr means 16 thousand years
ka	Thousands of (calendar) years ago	Ex. 16 ka means 16 thousand years before the present
LGM	Last Glacial Maximum	The last period in which global ice volume was at a maximum, generally corresponds to the last global mean sea level minimum (~26-21 thousand years ago)
LIS	Laurentide Ice Sheet	
MWP-1A	Meltwater Pulse 1a	A period of extreme sea level rise observed during the last deglacial period (discussed in detail in Ch. 2)
SMB	Surface Mass Balance	An ice-sheet’s surface mass balance is a measure of its accumulation/loss. A positive mass balance promotes ice sheet growth, a negative balance promotes retreat or ablation

TCN	Terrestrial <i>in-situ</i> cosmogenic nuclide	Unique isotopes produced during nuclear reactions between terrestrial atoms and cosmic rays (discussed in detail in section 5)
-----	---	--

**Table 2:** Organic  $^{14}\text{C}$  age-elevation pairs from the White Mountains, NH. Each age records the timing of revegetation in the sample location, and thus represents a minimum-limiting date for the ice surface vacating that location.

Site	Elev (m)	$^{14}\text{C}$ Age	cal yr BP	Source
<i>Moosilauke</i>				
Deer Lake bog	1325	13,000 $\pm$ 400	14,195-16,820	Spear (1989)
Mirror Lake	213	13,800 $\pm$ 560	15,720-17,415	Davis and Davis (1980)
<i>Franconia Notch</i>				
Lonesome Lake	831	10,535 $\pm$ 495	11,065-13,355	Spear et al. (1994)
Profile Lake	593	10,660 $\pm$ 40	12,772-12,885	Rogers (2003)
<i>Mt. Washington</i>				
Lakes of Clouds	1538	11,530 $\pm$ 165	10,790-13,355	Spear (1989)
Lost Pond	625	12,870 $\pm$ 370	14,580-15,760	Spear et al. (1994)

**Table 3:** New England dipstick sample locations,  $^{10}\text{Be}$  concentrations, and exposure ages. Uncertainties presented here are explained in detail in section 5.3. A density of 2.7 g cm $^{-3}$  was assumed for all samples.

Location	Sample	Lat	Lon	Elev (m)	Sample Thickness (cm)	Shielding Factor
Catskills	CAT-01	41.953	-74.398	1170.4	1.5	0.96652
Catskills	CAT-02	41.952	-74.398	1160.1	2	1
Catskills	CAT-03	41.951	-74.400	1122.0	2.5	0.97539
Catskills	CAT-04	41.944	-74.416	905.6	2.5	0.99757
Catskills	CAT-05	41.943	-74.416	900.1	2	0.98330
Jay Peak	JP-01	44.924	-72.526	1174.1	1.5	0.99988
Jay Peak	JP-02	44.924	-72.526	1174.1	2.5	1
Jay Peak	JP-03	44.924	-72.526	1174.1	3	1
Jay Peak	JP-04	44.922	-72.523	711.5	2	1
Jay Peak	JP-08	44.922	-72.523	1083.7	2	1
Jay Peak	JP-09	44.922	-72.522	1060.7	2	1
Jay Peak	JP-11	44.917	-72.511	830.8	1.5	1
Greylock	MG-01	42.641	-73.163	966.8	2	1
Greylock	MG-03	42.637	-73.165	1059.5	1	1

Greylock	MG-08	42.721	-73.174	406.9	4	0.94647
Greylock	MG-09	42.717	-73.174	387.1	5	0.98925
Mansfield	MMB-03	44.506	-72.861	411.1	2	1
Mansfield	MMB-02	44.506	-72.858	408.9	1.5	1
Mansfield	MM-19	44.524	-72.827	826.3	3.5	1
Mansfield	MM-17	44.519	-72.831	903.4	2.5	1
Mansfield	MM-16	44.519	-72.83	923.2	2	1
Franconia	FN-01	44.171	-71.683	623.5	2	0.91082
Franconia	FR-01	44.143	-71.644	1442.9	1	1
Franconia	LFT-13	44.161	-71.645	1597.5	2	0.99386
Franconia	LFT-14	44.161	-71.653	1353.9	2	0.97429
Franconia	LFT-18	44.154	-71.666	1086.9	2	0.98482
Franconia	AB-01	44.181	-71.695	661.9	2	0.99575
Franconia	AB-02	44.181	-71.695	661.9	2.5	0.99797
Franconia	FW-01	44.137	-71.671	710.8	1	0.94568
Franconia	LFT-10	44.161	-71.645	1597.5	2.5	0.99378
Franconia	LFT-12	44.161	-71.645	1597.5	1.5	0.99386
Franconia	LFT-15	44.159	-71.664	1250.9	2.5	0.94707
Killington	KM-03	43.605	-72.82	1288.7	1.5	1
Killington	KM-04	43.605	-72.82	1286.7	3	1
Killington	KM-05	43.611	-72.826	1040.7	1.5	0.98053
Killington	KM-06	43.614	-72.833	918.8	2	0.98989
Killington	KM-07	43.618	-72.839	772.8	4.5	1
Killington	KM-08	43.619	-72.868	598.8	3	0.97529
Killington	KM-09	43.619	-72.87	592.8	4	0.98604
Bigelow	BP-02	45.147	-70.288	1255.5	2	1
Bigelow	BP-03	45.147	-70.288	1255.5	3.5	1
Bigelow	BP-06	45.12	-70.317	499.7	3.5	1
Wachusett	WSP-05	42.503	-71.894	368.8	3	1

**Table 4:** Measured  $^{10}\text{Be}$  concentrations and calculated exposure ages for New England dipstick samples. Uncertainties presented here are explained in detail in section 5.3. Note:  $^{10}\text{Be}$  concentrations and uncertainties are presented using abbreviated scientific notation (i.e., E+05 =  $1 \times 10^5$ )

Location	Sample	$^{10}\text{Be}$ Conc. (atoms $\text{g}^{-1}$ )	$^{10}\text{Be}$ Conc. Unc (atoms $\text{g}^{-1}$ )	Exp Age (yr)	Int Unc (yr)	Ext Unc (yr)
Catskills	CAT-01	1.965E+05	4.193E+03	19461	417	1721
Catskills	CAT-02	1.986E+05	5.903E+03	19252	575	1749
Catskills	CAT-03	1.851E+05	4.666E+03	19030	482	1702

Catskills	CAT-04	1.508E+05	4.362E+03	18029	524	1632
Catskills	CAT-05	1.463E+05	4.013E+03	17747	489	1598
Jay Peak	JP-01	1.515E+05	4.256E+03	13605	384	1227
Jay Peak	JP-02	1.568E+05	4.685E+03	14200	426	1289
Jay Peak	JP-03	1.785E+05	5.186E+03	16240	474	1470
Jay Peak	JP-04	1.185E+05	3.648E+03	11491	355	1046
Jay Peak	JP-08	1.173E+05	4.210E+03	11374	409	1056
Jay Peak	JP-09	5.030E+04	4.487E+03	4962	443	613
Jay Peak	JP-11	1.402E+05	4.733E+03	16709	566	1540
Greylock	MG-01	1.332E+05	1.053E+04	14836	1177	1733
Greylock	MG-03	1.529E+05	4.237E+03	15679	436	1413
Greylock	MG-08	6.993E+04	3.041E+03	13367	583	1285
Greylock	MG-09	7.763E+04	2.765E+03	14582	521	1354
Mansfield	MMB-03	7.664E+04	3.058E+03	13258	531	1254
Mansfield	MMB-02	7.862E+04	3.305E+03	13857	585	887
Mansfield	MM-19	1.026E+05	3.355E+03	12553	412	1151
Mansfield	MM-17	1.251E+05	4.195E+03	14243	479	1311
Mansfield	MM-16	1.126E+05	4.340E+03	12553	485	1179
Franconia	FN-01	7.935E+04	2.859E+03	12272	444	1141
Franconia	FR-01	1.991E+06	2.077E+04	151188	1638	13506
Franconia	LFT-13	3.843E+05	1.009E+04	25326	669	2276
Franconia	LFT-14	1.622E+05	6.380E+03	12857	507	1212
Franconia	LFT-18	1.023E+05	4.836E+03	10023	475	980
Franconia	AB-01	9.208E+04	2.951E+03	13190	424	763
Franconia	AB-02	9.388E+04	4.353E+03	13147	612	1281
Franconia	FW-01	9.540E+04	3.936E+03	12664	524	1204
Franconia	LFT-10	3.588E+05	8.526E+03	23734	567	2116
Franconia	LFT-12	7.695E+05	1.409E+04	50821	942	4494
Franconia	LFT-15	1.560E+05	4.750E+03	14601	446	833
Killington	KM-03	1.736E+05	4.703E+03	14614	397	1314
Killington	KM-04	1.767E+05	4.808E+03	15088	412	1357
Killington	KM-05	1.013E+05	3.488E+03	10858	375	643
Killington	KM-06	8.326E+04	3.293E+03	9794	388	610
Killington	KM-07	1.150E+05	2.877E+03	15075	379	1346
Killington	KM-08	8.209E+04	4.647E+03	12886	732	959
Killington	KM-09	1.219E+05	7.003E+03	19215	1109	1445
Bigelow	BP-02	3.247E+05	7.928E+03	27321	672	2442
Bigelow	BP-03	2.091E+05	5.624E+03	17772	480	1598
Bigelow	BP-06	8.816E+04	3.756E+03	14103	603	1350

Wachusett	WSP-05	8.353E+04	4.077E+03	15543	762	1534
-----------	--------	-----------	-----------	-------	-----	------

**Table 5:** Mt. Mansfield samples collected and processed by Lee Corbett, Paul Bierman, Thom Davis, Jeremy Shakun, and Alexandria Koester.

Sample	Latitude	Longitude	Elev (m)	Exp. Age (Yr)	Int. Uncertainty (yr)	Ext. Uncertainty (yr)
MM-01	44.53032	-72.81718	1164	14569	270	752
MM-02	44.53062	-72.81691	1172	15254	283	787
MM-03	44.53357	-72.81697	1176	14032	260	724
MM-04	44.53347	-72.81689	1174	14135	262	729
MM-05	44.53475	-72.81730	1180	13983	259	721
MM-06	44.53608	-72.81732	1197	14522	269	749
MM-07	44.53608	-72.81738	1197	14216	311	752
MM-08	44.54369	-72.81434	1305	18388	338	948
MM-09	44.54289	-72.81486	1300	24778	532	1309
MM-10	44.54320	-72.81591	1297	16995	336	885
MM-11	44.54200	-72.81526	1270	15703	290	810
MM-12	44.54389	-72.81837	1226	18931	467	1025
MM-13	44.54371	-72.82078	1174	15090	280	779
MM-14	44.54264	-72.82317	1090	14108	416	796
MM-15	44.54232	-72.82639	1025	14527	270	750

**Table 6:** The onset of exposure from each sample location based on Monte Carlo simulations

Location	Latitude North (approximate)	Highest Elevation Sample (m)	Earliest Exposure (ka, with 1 $\sigma$ uncertainty)
Catskills, NY	41.9	1,170	19.46 $\pm$ 0.41
Wachusett, MA	42.5	369	15.54 $\pm$ 0.76
Greylock, MA	42.7	1,060	15.68 $\pm$ 0.44
Killington, VT	43.6	1,288	14.99 $\pm$ 0.28
Franconia Notch, NH	44.2	1,354	13.73 $\pm$ 0.35
Mansfield, VT	44.5	1,200	14.37 $\pm$ 0.10

## Figures



**Figure 2:** A recent reconstruction of the Laurentide Ice Sheet at its maximum extent (from Stokes, 2017). The red box shows the area of focus for this project. Also shown are 117 hypothesized ice streams (dark blue with flow lines) based on Margold et al. (2015).

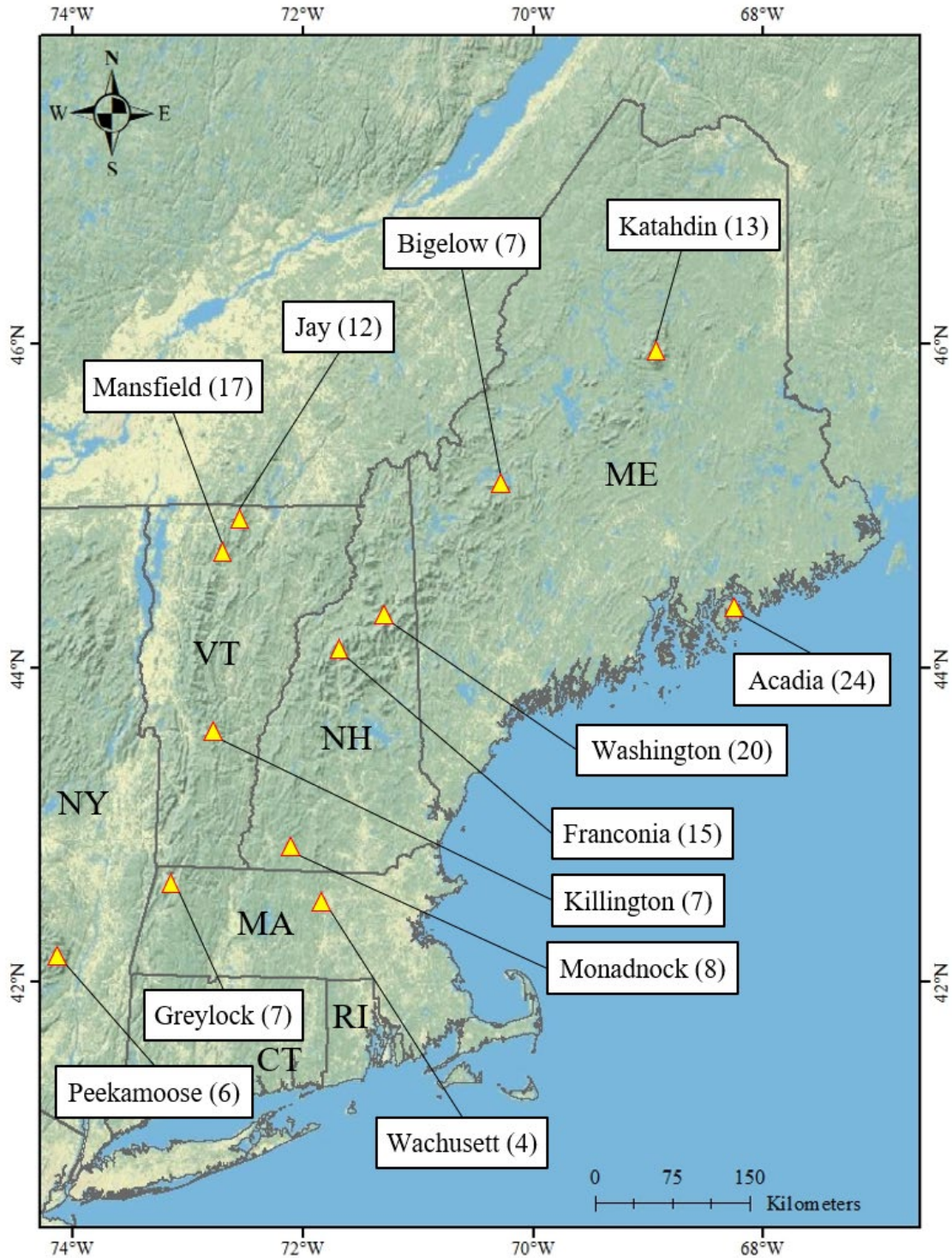


**Figure 2:** Map of dipstick sample locations in New England (locations are described in section 5.1.2). Numbers in parentheses indicate the number of samples collected at each location. Koester et al. (2017, *in prep*) produced dipsticks for Acadia National Park, ME and Mt. Washington, NH. Davis et al. (2015) produced a dipstick for Mt. Katahdin, ME. Note: Mt. Monadnock does not currently have any exposure ages calculated, but samples have been collected.

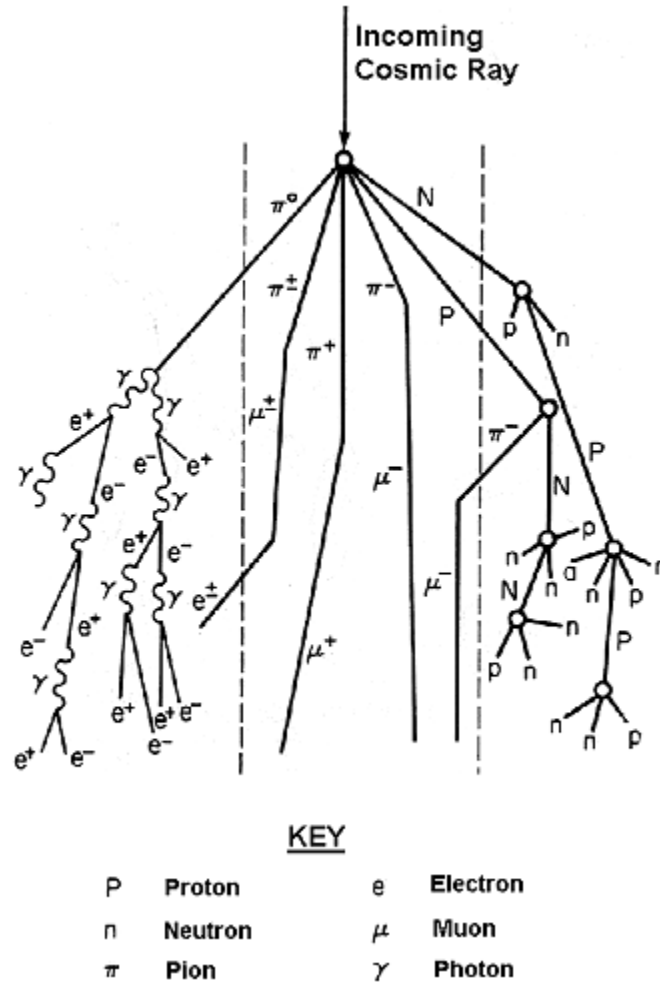


**Figure 3:** Visualization of an incident primary cosmic particle and the secondary cosmic particle cascade (from Gosse and Phillips, 2001). To illustrate the three main components of the secondary cascade, this figure is split into three panels. The leftmost panel shows the electromagnetic component, the middle shows the mesonic component, and the right panel shows the nucleonic, or hadronic, component. The nucleonic component is mainly responsible for causing further collisions with other atmospheric or terrestrial atoms, expanding the cascade.

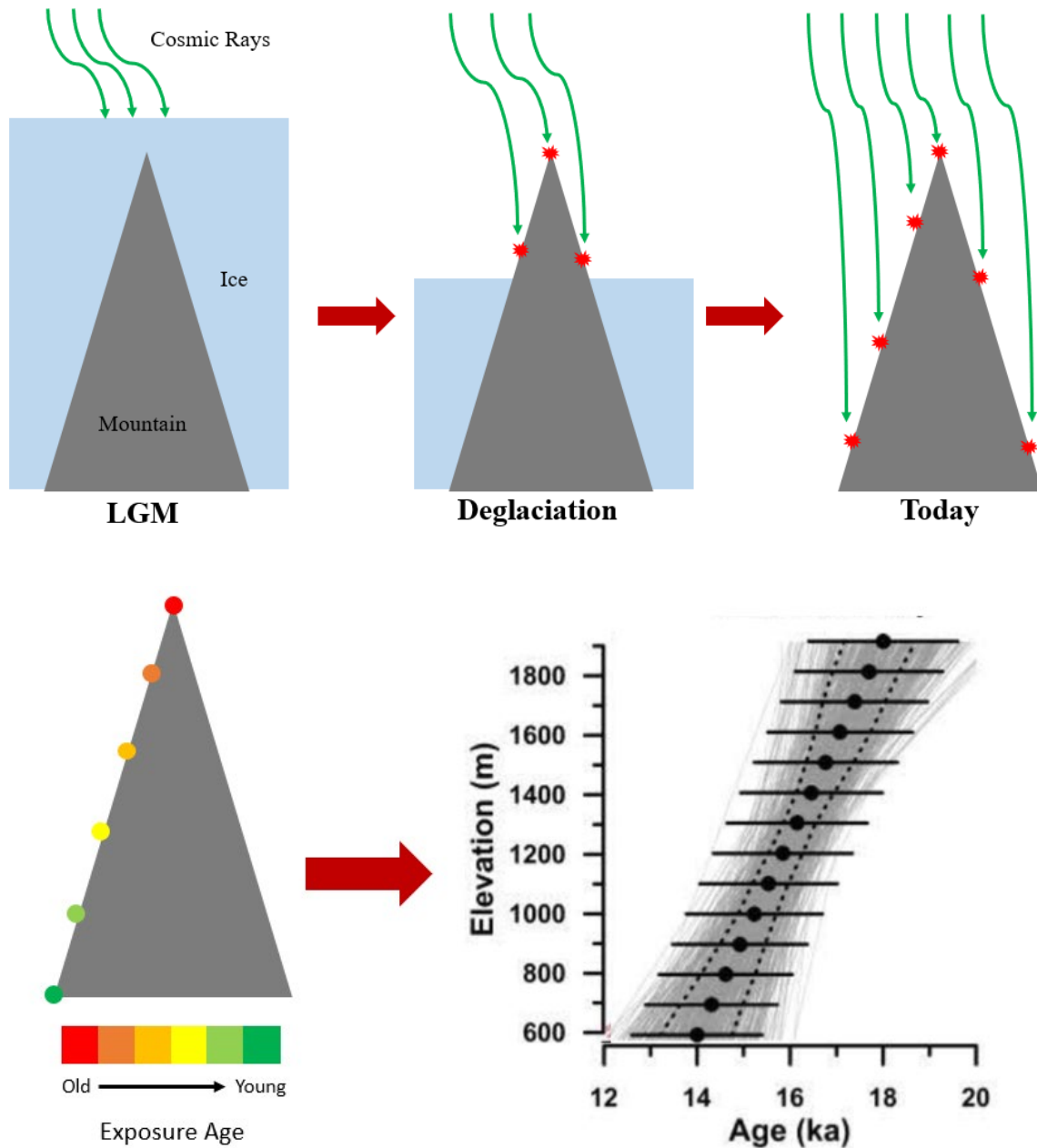


**Figure 4:** A simplified depiction of the dipstick method. Green lines in top panel are cosmic rays, while red starbursts represent the formation of terrestrial *in-situ* cosmogenic nuclides. Top-left panel: at the LGM, every mountain in New England was covered by the Laurentide Ice Sheet, blocking cosmic rays from interacting with surficial minerals. Top-middle panel: as the Laurentide began to thin, cosmic rays could interact with minerals near the top of the mountain, forming TCNs at higher elevations only. Top-right panel: today, every peak in New England is deglaciated, and TCNs form at all elevations. Bottom-left panel: typical expected exposure age profile from a mountain in New England, due to early exposure of higher elevations. Bottom-right panel: an example of a ‘dipstick’ plot using synthetic data. The plot shows exposure age on the x-axis vs. elevation on the y-axis. Monte-carlo analyses (grey lines) using the measurement uncertainty on each point (error bars) give a population of possible thinning timing and rates.

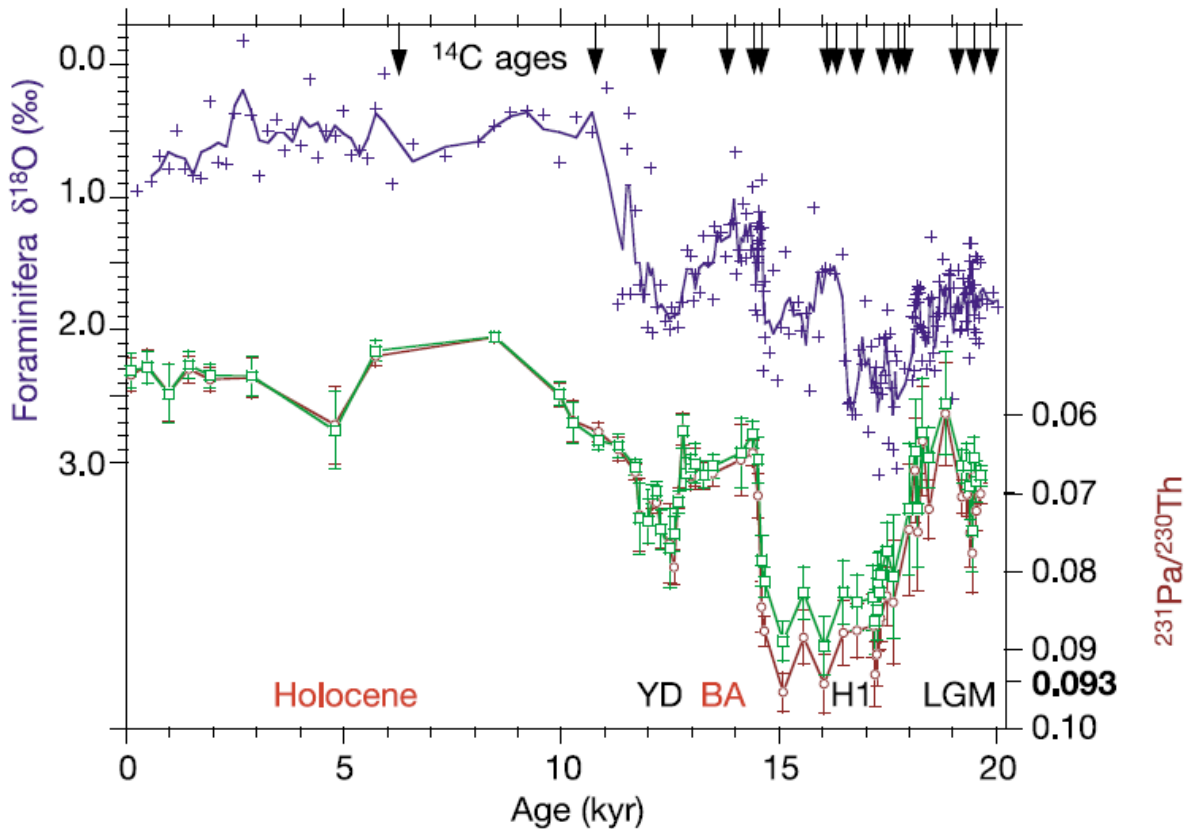


**Figure 5:** Proxy data from a high-accumulation-rate core from the Bermuda rise in the western subtropical Atlantic spanning the last 20 kyr (from McManus et al., 2004). The top record shows individual measurements (blue crosses) and the three-point running mean (blue line) of planktonic foraminifera  $\delta^{18}\text{O}$  (*G. inflata*). This record is used as a proxy for ocean temperature, with lower values (higher on plot due to inverted axis) indicating higher temperatures and vice versa. The bottom plot shows sedimentary  $^{231}\text{Pa}/^{230}\text{Th}$ , a kinematic proxy that is used to determine times of vigorous ocean convection (low values, higher on this plot due to an inverted axis) vs. times of little to no ocean convection (high values, lower on this plot due to an inverted axis). Also shown are  $^{14}\text{C}$  age control points (arrows) and significant climatic intervals (labelled above x axis).

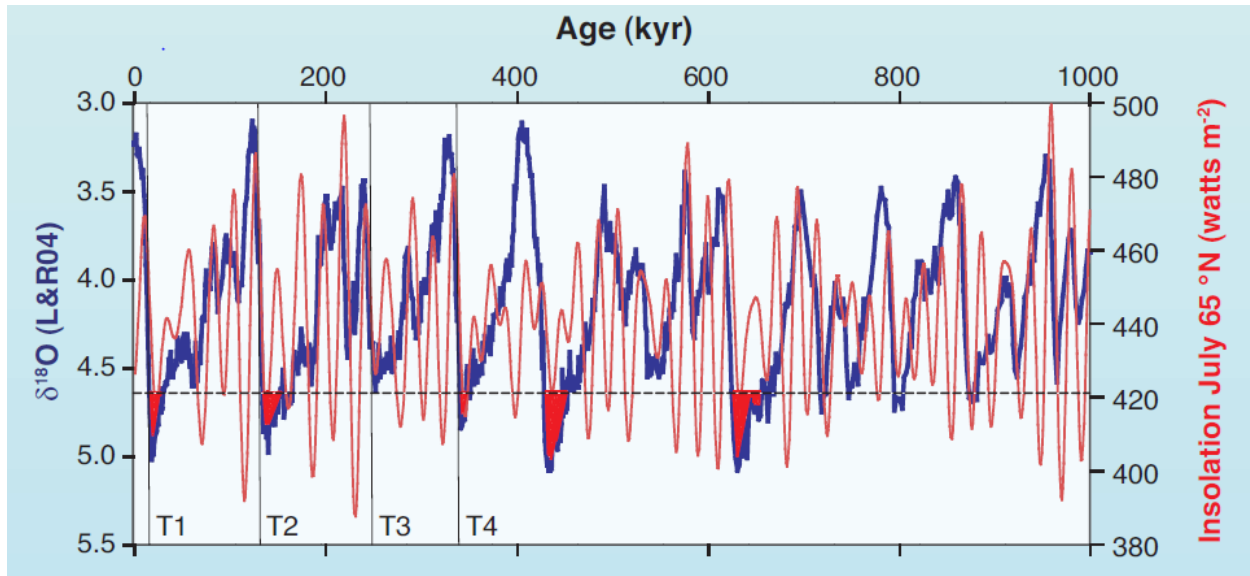


**Figure 6:** A benthic foraminifera oxygen-isotopic record (blue line), a proxy for global ice volume, compared to July insolation at 65°N (red line) over the past 1 million years (from Denton et al., 2010). The dashed line with red shading below it represents the “tipping point”, past which global ice volume is so large that relatively small forcings can trigger rapid retreat. Major terminations that are widely studied are labeled (T1-T4). Of particular note in this figure is the “sawtooth” pattern of long periods of increasing ice volume followed by rapid deglaciations, which does not completely match the more sinusoidal insolation curve.

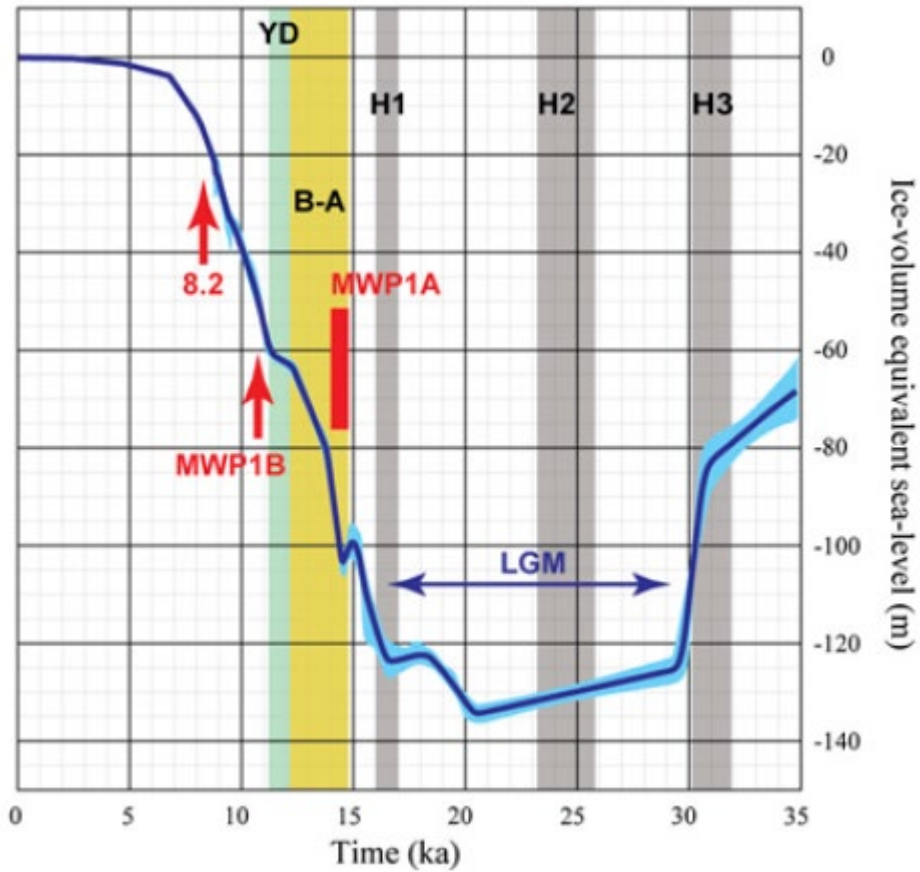


**Figure 7:** Global eustatic sea level reconstruction of the last 35 kyr (from Lambeck et al., 2014). This reconstruction is based on a compilation of far-field sea-level proxy indicators. The dark blue line shows the most-likely ESL estimate through time, and the light blue shaded area shows the 95% probability limiting values. Significant events from this time period are labelled, including: Heinrich Events 1, 2, and 3 (H1, H2, H3), the Last Glacial Maximum (LGM), Meltwater Pulse 1a (MWP1A), the Bølling-Allerød warm period (B-A), Meltwater Pulse 1B (MWP1B), the Younger Dryas (YD), and the 8.2k event (8.2).

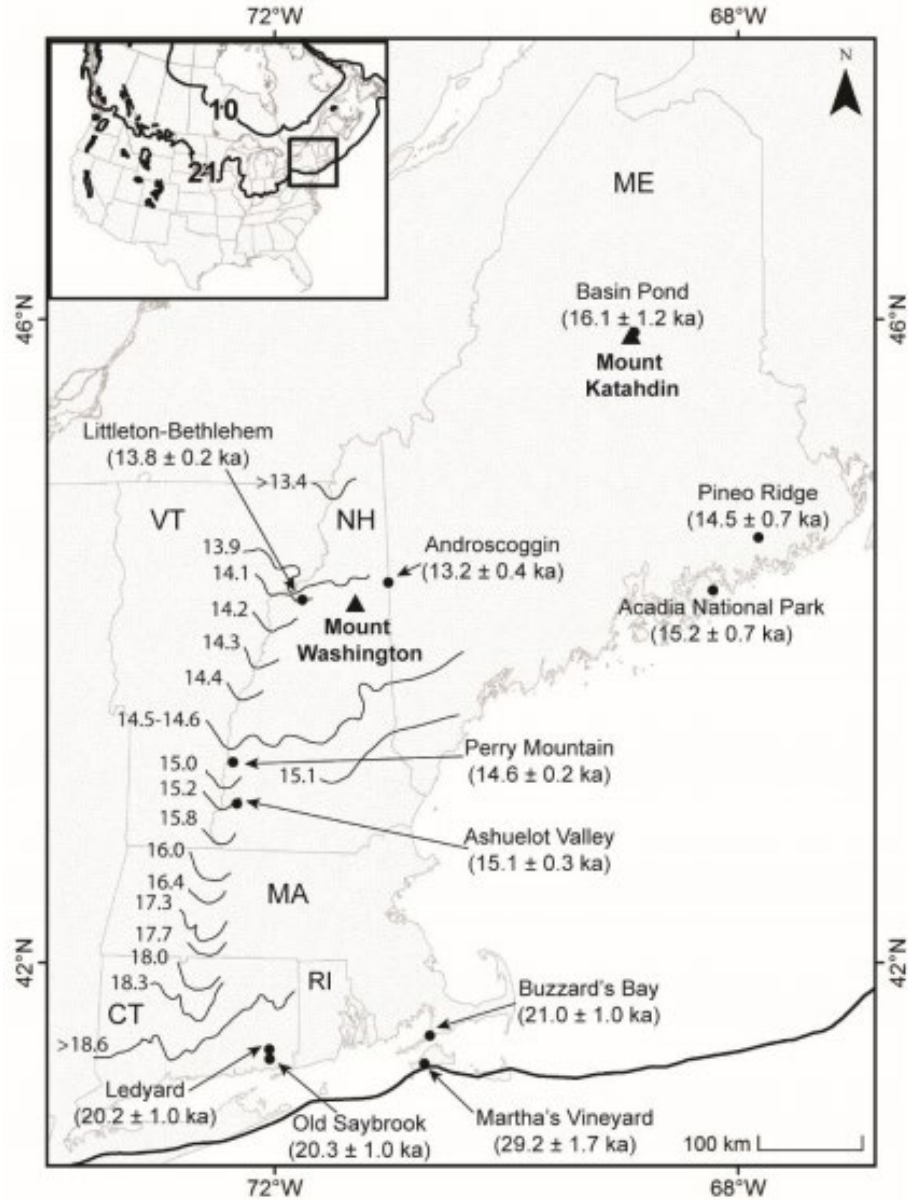


**Figure 8:** Constraints on the southeastern LIS retreat history through New England (from Davis et al. 2017). Isochrons show the North American Varve Chronology (Ridge et al., 2012), each line represents a position of the LIS margin, and the number next to it is date (ka) at which the margin was at that position. Black dots show <sup>10</sup>Be exposure ages for glacial landforms (Martha's Vineyard and Buzzard's Bay – Balco et al., 2002; Old Saybrook and Ledyard – Balco and Schaefer, 2006; Ashuelot Valley, Perry Mountain and Littleton-Bethlehem – Balco et al., 2009; Bromley et al., 2015; Basin Pond – Davis et al., 2015; Pineo Ridge and Acadia National Park – Koester et al., 2017). Inset figure shows the extent of the LIS at 21 ka and 10 ka (Dyke, 2004)

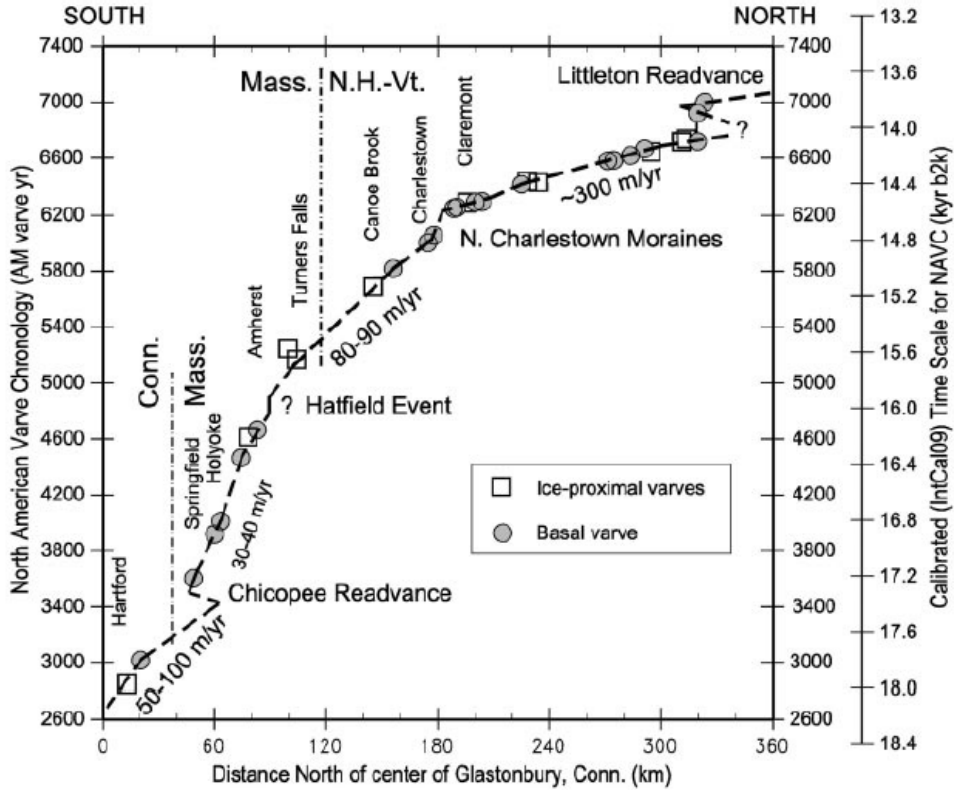


**Figure 9:** Time distance plot of LIS recession up the Connecticut Valley based on the new North American Varve Chronology (Ridge et al., 2012).



**Figure 10:** Embedded pebbles in a conglomerate boulder from the eastern Catskill Mountains, NY. In this photo, one pebble has been knocked out of the boulder with a chisel and hammer (finger is pointing to the crater).



**Figure 11:** A prominent quartz vein from the summit of Jay Peak, VT. The arrow on the scale card is 10 cm long.



**Figure 12:** Example of a prominent quartz vein on Mt. Mansfield, VT.

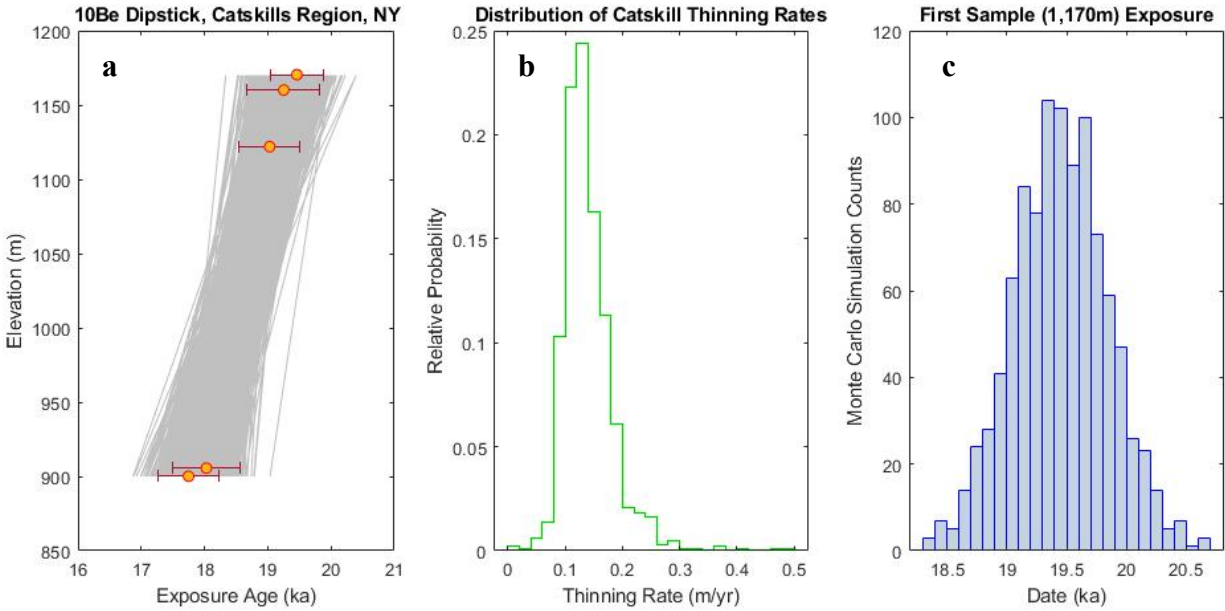


**Figure 13:** Results of Monte Carlo dipstick simulations using exposure ages from the Catskill Mountains, NY. (a) Exposure ages with  $1\sigma$  measurement uncertainties as well as individual Monte Carlo dipstick simulations (gray lines). (b) Probability distribution of simulated thinning rates. (c) Distribution of exposure ages for the highest elevation captured by the Catskills dipstick.

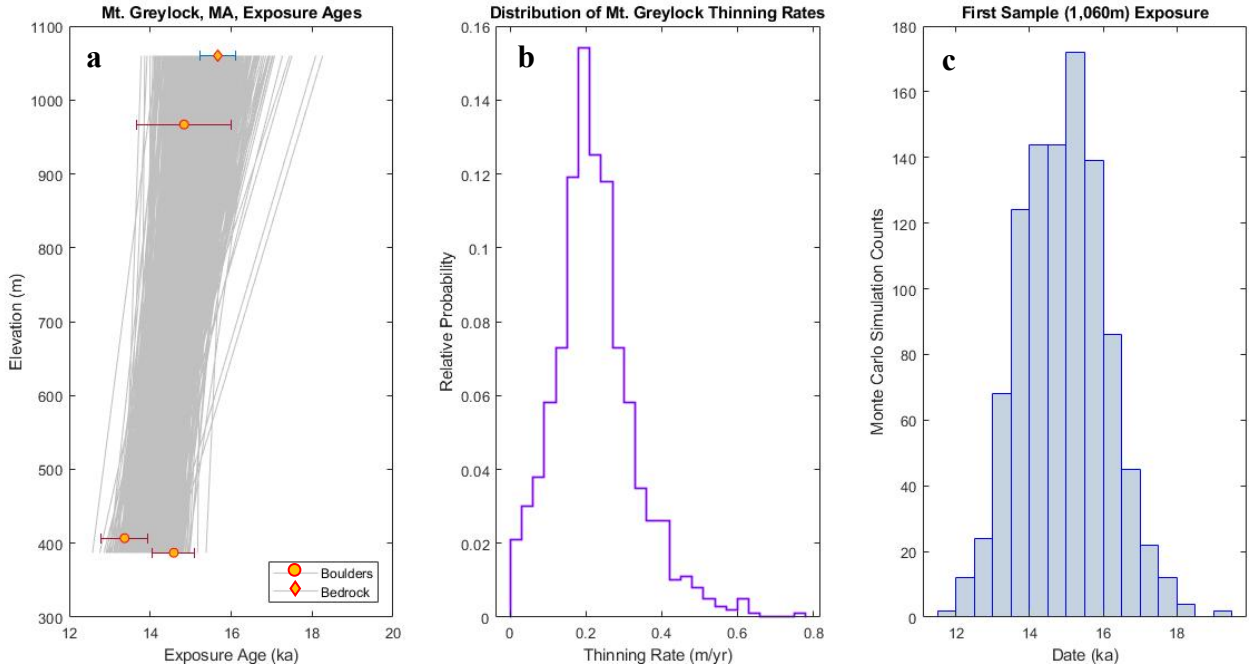


**Figure 14:** Results of Monte Carlo dipstick simulations using exposure ages from Mt. Greylock, MA. (a) Exposure ages with  $1\sigma$  measurement uncertainties as well as individual Monte Carlo dipstick simulations (gray lines). (b) Probability distribution of simulated thinning rates. (c) Distribution of exposure ages for the highest elevation captured by the Mt. Greylock dipstick

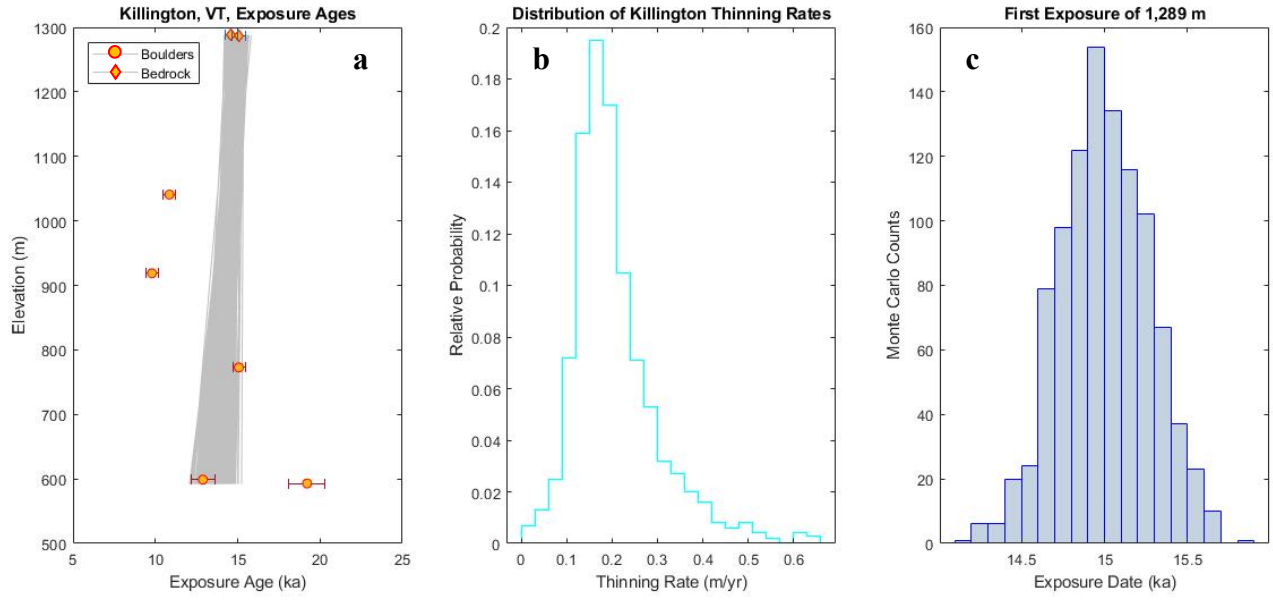


**Figure 15:** Results of Monte Carlo dipstick simulations using exposure ages from Killington Mt., VT. (a) Exposure ages with  $1\sigma$  measurement uncertainties as well as individual Monte Carlo dipstick simulations (gray lines). (b) Probability distribution for the simulated thinning rates. (c) Distribution of exposure ages for the highest elevation captured by the Killington dipstick

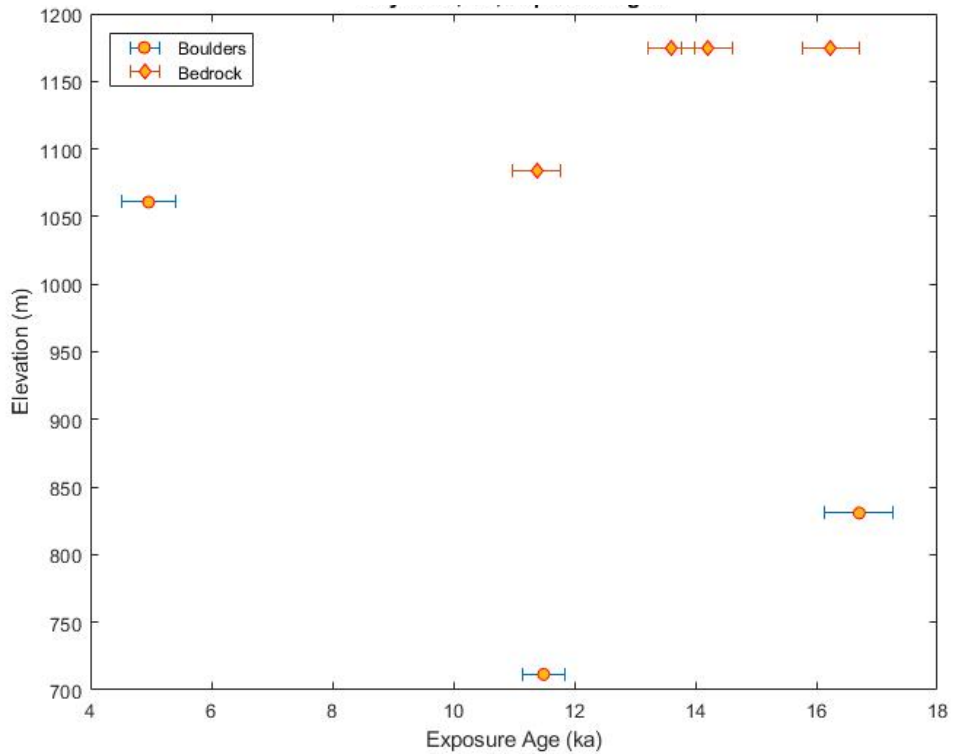


**Figure 16:** Exposure ages from Jay Peak, VT with  $1\sigma$  internal uncertainties.

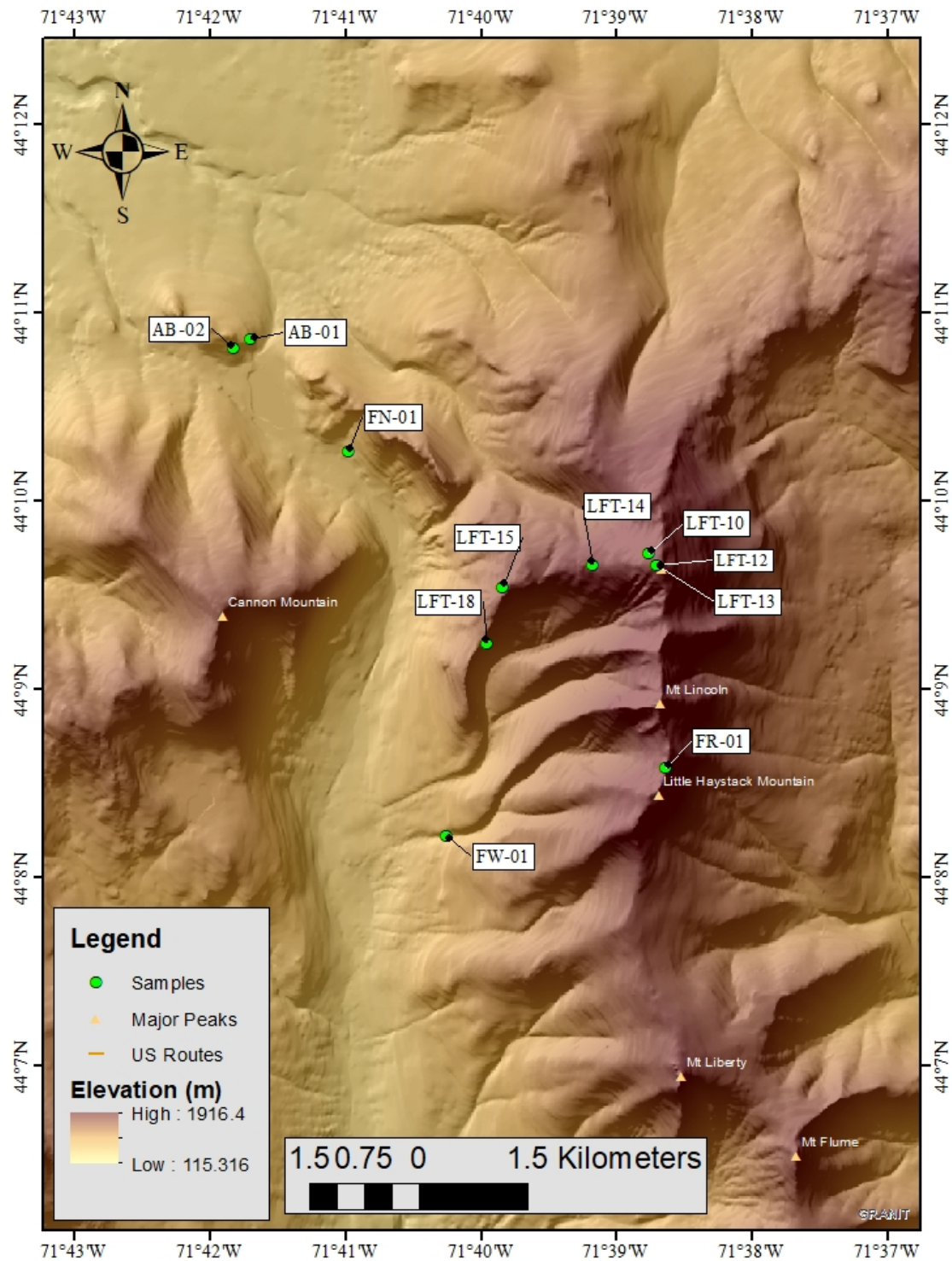


**Figure 17:** Franconia Notch sample locations. Note, LFT-10, 12, and 13 are from the summit of Mt. Lafayette.

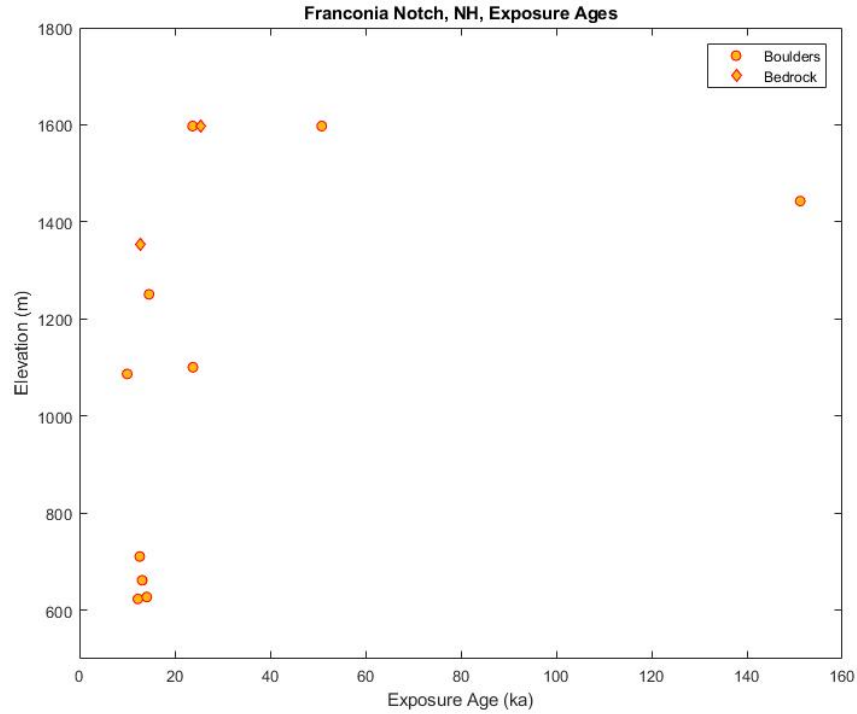


**Figure 18:** Exposure ages from Franconia Notch, NH.

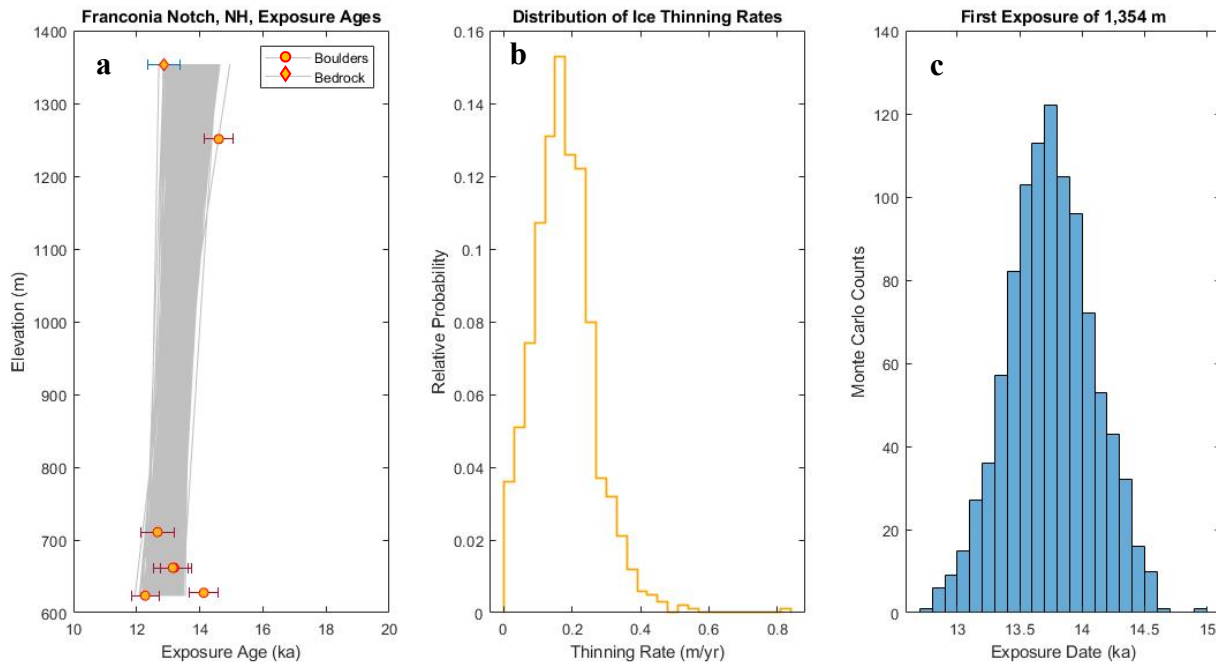


**Figure 19:** Results of Monte Carlo dipstick simulations using exposure ages from Franconia Notch, NH. (a) Exposure ages with  $1\sigma$  measurement uncertainty as well as individual Monte Carlo dipstick simulations (gray lines). (b) Probability distribution for the simulated thinning rates. (c) Distribution of exposure ages for the highest elevation captured by the Franconia Notch dipstick



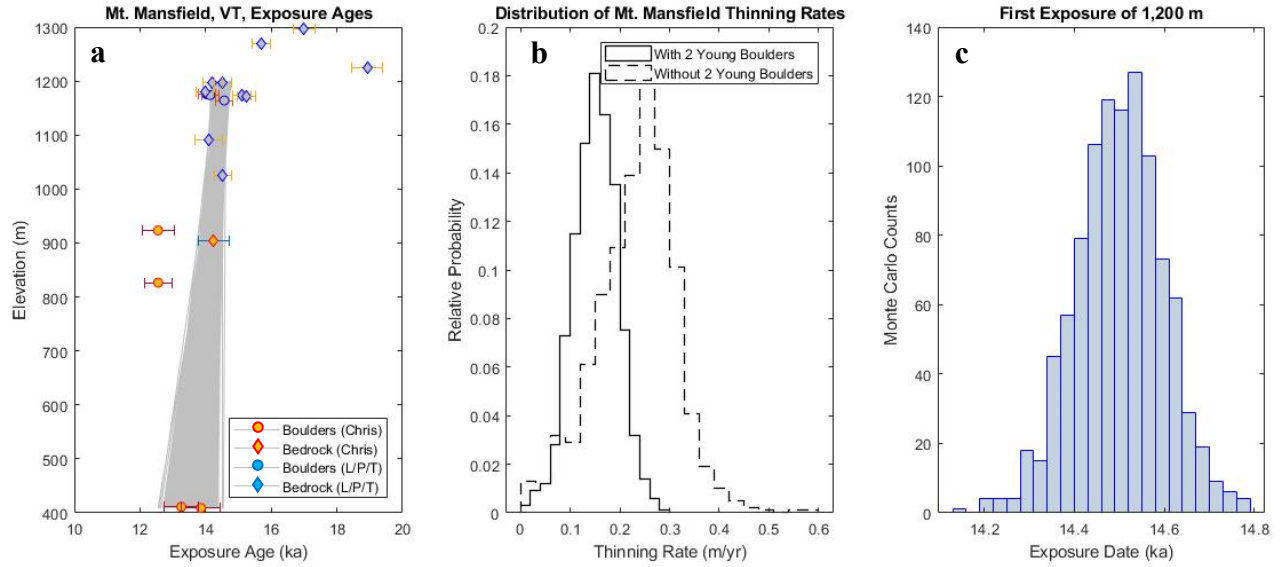


**Figure 21:** Results of Monte Carlo dipstick simulations using exposure ages from Mt. Mansfield, VT. (a) Exposure ages with  $1\sigma$  measurement uncertainty as well as individual Monte Carlo dipstick simulations (gray lines). Orange ages were collected and processed by the author, blue ages were collected and processed by Lee Corbett, Paul Bierman, P. Thompson Davis, Jeremy Shakun, and Allie Koester (b) Probability distribution for the simulated thinning rates with (solid line) and without (dashed line) two young boulder ages from mid-elevations. (c) Distribution of exposure ages for the highest elevation captured by the Mt. Mansfield dipstick

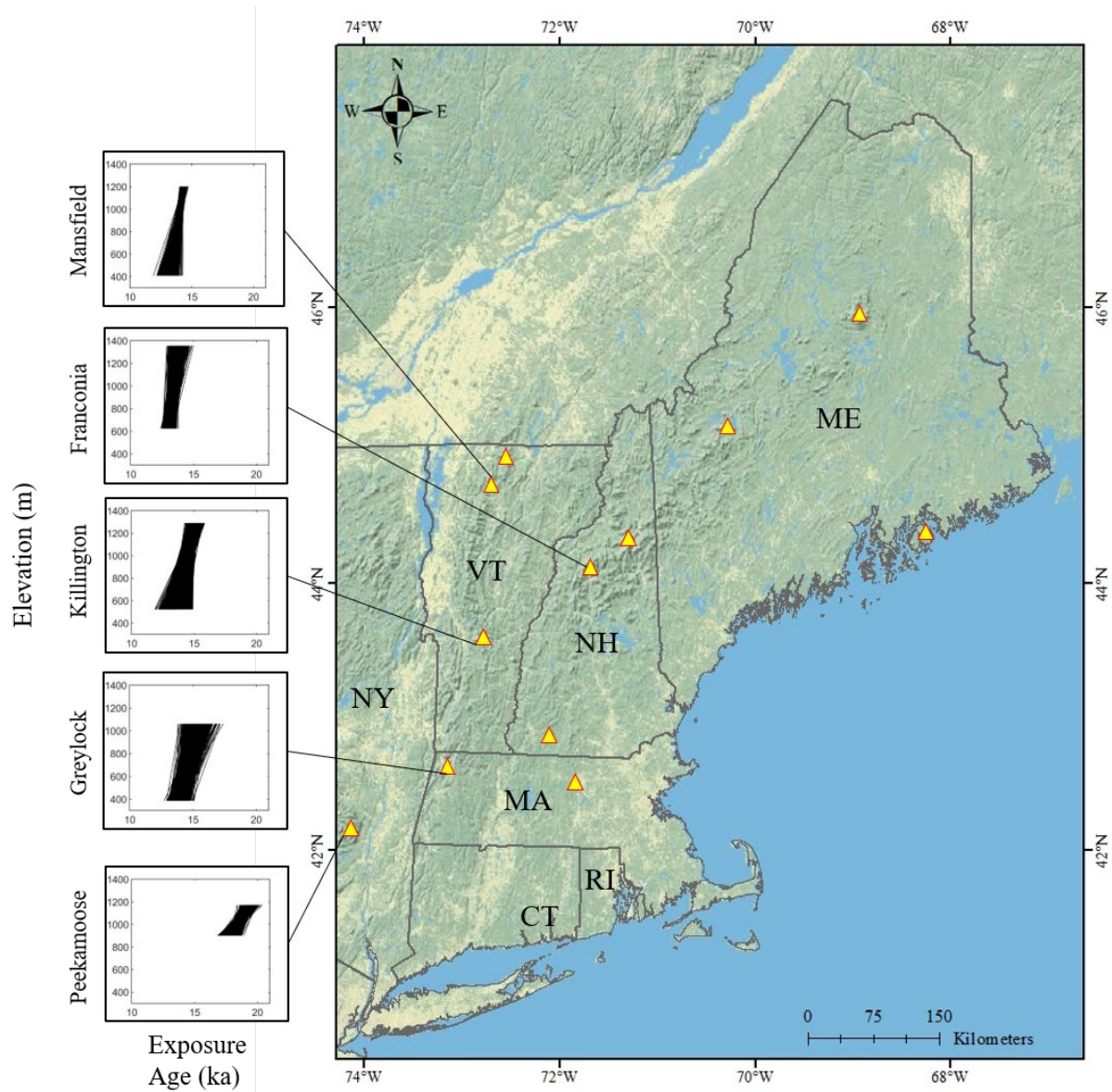


**Figure 32:** Preliminary dipsticks in the northeastern United States. All plots have consistent axes: x-axis shows exposure age from 20-10 ka, y-axis shows elevation from 400 to 1400 m a.s.l. Individual data points are not shown for each dipstick, but the individual Monte Carlo simulations are presented (thin black lines)